Mineralium Deposita (2023) 58:1101–1122
https://doi.org/10.1007/s00126-023-01170-2

ARTICLE

Sources, transport, and deposition of metal(loid)s recorded by sulfide and rock geochemistry: constraints from a vertical profile through the epithermal Profitis Ilias Au prospect, Milos Island, Greece

Anna Grosche[1] · Reiner Klemd[1] · Katja Denkel[1] · Manuel Keith[1] · Karsten M. Haase[1] · Panagiotis C. Voudouris[2] · Dimitrios Alfieris[3] · Michael Wiedenbeck[4]

Received: 9 August 2022 / Accepted: 14 March 2023 / Published online: 1 April 2023

Abstract

Drill core samples from the Profitis Ilias Pb-Zn-Cu-Ag-Au vein mineralization on Milos Island, Greece provide new insights into (i) the metal sources, (ii) the primary vertical metal(loid) distribution, and (iii) the supergene enrichment processes in a transitional shallow-marine to subaerial hydrothermal environment. Metal contents of unaltered and altered host rocks combined with Pb isotope analyses of hydrothermal sulfides suggest that most metal(loid)s were derived by leaching of basement rocks, whereas the distinct enrichment of Te is related to the addition of Te by a magmatic fluid. The trace element contents of base metal sulfides record decreasing Au, Te, Se, and Co, but increasing Ag, Sb, and Tl concentrations with increasing elevation that can be related to progressive cooling and fluid boiling during the hypogene stage. The formation of base metal veins with porous pyrite hosting hessite inclusions at ~ 400 m below the surface was triggered by vigorous fluid boiling. By contrast, the enrichment of native Au associated with oxidized Fe and Cu phases in the shallower part of the hydrothermal system resulted from supergene remobilization of trace Au by oxidizing meteoric water after tectonic exhumation to subaerial levels. Disseminated pyrite with higher Tl/Pb ratios and locally elevated Hg concentrations relative to vein pyrite reflects infiltration of the host rocks by boiled liquids and condensed vapor fluids. The vertical and temporal evolution of the Profitis Ilias mineralization, therefore, provides unique insights into the transport and precipitation of Au, Ag, Te, and related metal(loid)s by multiple fluid processes.

Keywords Epithermal deposits · Boiling · Supergene enrichment · Tellurium · Gold

Introduction

Magmatic-hydrothermal systems in subduction zone environments are important contributors to the world's Cu, Au, Pb, Zn, Ag, and Mo supply (Hedenquist and Lowenstern 1994). In addition, arc-related epithermal and volcanogenic massive sulfide deposits in the shallow crust and associated hybrid mineralization-styles exhibit significant enrichments of metals and metalloids (summarized as metal(loid)s) with a volatile affinity, such as As, Sb, Tl, Te, Bi, Hg, and Se (Saunders and Brueseke 2012; Goldfarb et al. 2016). Yet, our understanding of the behavior of these elements in hydrothermal solutions remains incomplete, as the processes controlling their enrichment are complex.

The formation of local metal(loid) enrichments in hydrothermal systems results from an interplay of the fluid and metal sources combined with suitable conditions for the transport and deposition of these elements (Hemley and Hunt

Editorial handling: D. Dolejs

✉ Anna Grosche
anna.grosche@fau.de

[1] GeoZentrum Nordbayern, Friedrich-Alexander-Universität (FAU) Erlangen-Nürnberg, Schlossgarten 5, 91054 Erlangen, Germany

[2] Faculty of Geology & Geoenvironment, National and Kapodistrian University of Athens, 15784 Athens, Greece

[3] Research and Consulting Geoscientist at DALFEX, Athens, Greece

[4] Deutsches GeoForschungsZentrum GFZ, 14473 Potsdam, Germany

1992; Hedenquist and Lowenstern 1994). Yet, metal sources are often difficult to define and the contribution of magmatic fluids to the metal budget of hydrothermal systems associated with volcanic rocks is a key issue in subduction-related systems (Richards 2011; Keith et al. 2018a; Martin et al. 2020; Falkenberg et al. 2022). Combined trace element and isotope analyses (e.g., Pb and S) of hydrothermal precipitates provide further insights into the metal sources and fluid processes that control the enrichment of key elements in mineral deposits (Berkenbosch et al. 2019; Wind et al. 2020; Klose et al. 2021; Falkenberg et al. 2021; Schaarschmidt et al. 2021a).

Starting with a metal-rich, hot fluid at depth, the transport of metal(loid)s during ascent is controlled by the physicochemical fluid properties including temperature, pressure, pH, salinity, oxygen fugacity (fO_2), and sulfur fugacity (fS_2). The evolving conditions during ascent of a fluid determine the speciation, and, thus, the solubility of the dissolved components (Crerar et al. 1985; Hemley et al. 1992; Einaudi et al. 2003; Pokrovski et al. 2013). Numerical modeling, experimental data, and observations in natural systems have shown that changing fluid conditions resulting from mixing, boiling, or fluid-rock interaction trigger metal deposition in hydrothermal systems (Drummond and Ohmoto 1985; Cooke and McPhail 2001; Reed and Palandri 2006; Heinrich 2007; Simmons et al. 2016). Therefore, trace element composition in hydrothermal sulfides is useful for characterizing conditions and processes during metal deposition (Frenzel et al. 2016; Keith et al. 2018b; Román et al. 2019; Steadman et al. 2021; Falkenberg et al. 2021). Sulfides from different hydrothermal sites, different depth, or different hydrothermal stages record distinct fluid processes through space and time during the formation of multistage or zoned mineralization (Román et al. 2019; Grant et al. 2020; Frenzel et al. 2021; Swinkels et al. 2021; Wang et al. 2022; Falkenberg et al. 2022).

Drill core samples from the Profitis Ilias Pb-Zn-Cu-Ag-Au mineralization in western Milos, Greece span a depth range of > 500 m, providing a vertical profile through a young (< 3 Ma) multi-stage epithermal system in a volcanic arc setting. Previous studies focused on the mineralogical and thermobarometric characterization of the system. These showed that boiling conditions during fluid ascent controlled the deposition of both base metals and native gold (Kilias et al. 2001; Naden et al. 2003; Alfieris et al. 2013). Here, we use a multi-analytical approach to investigate the metal budget, the metal sources, and the vertical distribution of metals within the mineralized rocks by examining the trace element and isotopic composition of both base metal sulfides and altered host rocks. This allows us to define the temporal and vertical fluid evolution, which can be linked to physicochemical changes during fluid cooling, boiling, and supergene overprint.

Geological setting of Milos Island and the Profitis Ilias Au prospect

Milos Island (Fig. 1) is located within the South Aegean Volcanic Arc (SAVA), where the African plate is subducting towards the north beneath the Aegean microplate in the eastern Mediterranean. The island largely consists of Pliocene to recent volcanic and volcaniclastic units (Fig. 1) that overly the metamorphic basement and some Neogene marine sediments (Fytikas et al. 1986). The metamorphic basement is dominated by Mesozoic greenschist- to blueschist-facies metasediments of the Cycladic Blueschist Unit (Liakopoulos et al. 1991; Grasemann et al. 2018). The volcanism shows a general evolution from submarine pyroclastic activity (3.3 to 2.13 Ma) and submarine eruption of andesitic to rhyolitic lavas (2.13 to 1.48 Ma) to subaerial rhyolitic activity (1.48 Ma to present) (Stewart and McPhie 2006; Zhou et al. 2021). Hydrothermal activity led to the formation of several hybrid epithermal-VMS-style Pb-Zn-Cu-Ag-Au vein mineralization across western Milos (Naden et al. 2005; Alfieris et al. 2013; Schaarschmidt et al. 2021a). Recent hydrothermal activity such as shallow-submarine venting of metal-rich fluids with temperatures up to 115 °C at Paleochori Bay in the southeast of Milos Island (Valsami-Jones et al. 2005) is located along NW–SE striking tectonically active graben structures (Fig. 1).

Profitis Ilias (Fig. 1) represents the highest elevation of the island (748 m) and displays vein mineralization, which was prospected for Au during a drilling program in 1994. The Pb-Zn-Cu-Ag-Au mineralization at Profitis Ilias has been estimated to contain five million tons of ore with 4.4 g/t Au and 43 g/t Ag and has been the subject of several studies (Kilias et al. 2001; Naden et al. 2005; Alfieris et al. 2013). Drill cores crosscut the dacitic-rhyolitic cryptodome that forms the core of the volcanic center and is surrounded by the voluminous Profitis Ilias ignimbrite, which is a submarine pumice breccia (Fig. 2a). A recent study dated the Profitis Ilias cryptodome and the pumice breccia to 2.75 and 2.62 Ma, respectively (Miles 2021). Two drill cores reached the contact to the underlying metamorphic basement at 180 and 230 m (all elevations given in meters above sea level). In one of these drill cores (PD11), the basement is overlain by a ~ 10 m thick layer of Neogene sedimentary rocks and two 25 m thick tuff units (Fig. 2a) that are related to submarine explosive volcanic activity during the Late Pliocene. The different lithological units of Profitis Ilias are intersected by complex, mostly N-S and NE-SW striking veins that host the Pb-Zn-Cu-Ag-Au mineralization (Kilias et al. 2001). The surface alteration of Profitis Ilias consists of an argillic alteration assemblage comprising illite ± kaolinite ± smectite ± sericite, while the epithermal veins are surrounded by adularia-sericite alteration (Alfieris et al. 2013).

Previous studies at Profitis Ilias revealed vertical trends in the mineralogy, the Au and Ag grades, and the fluid temperature

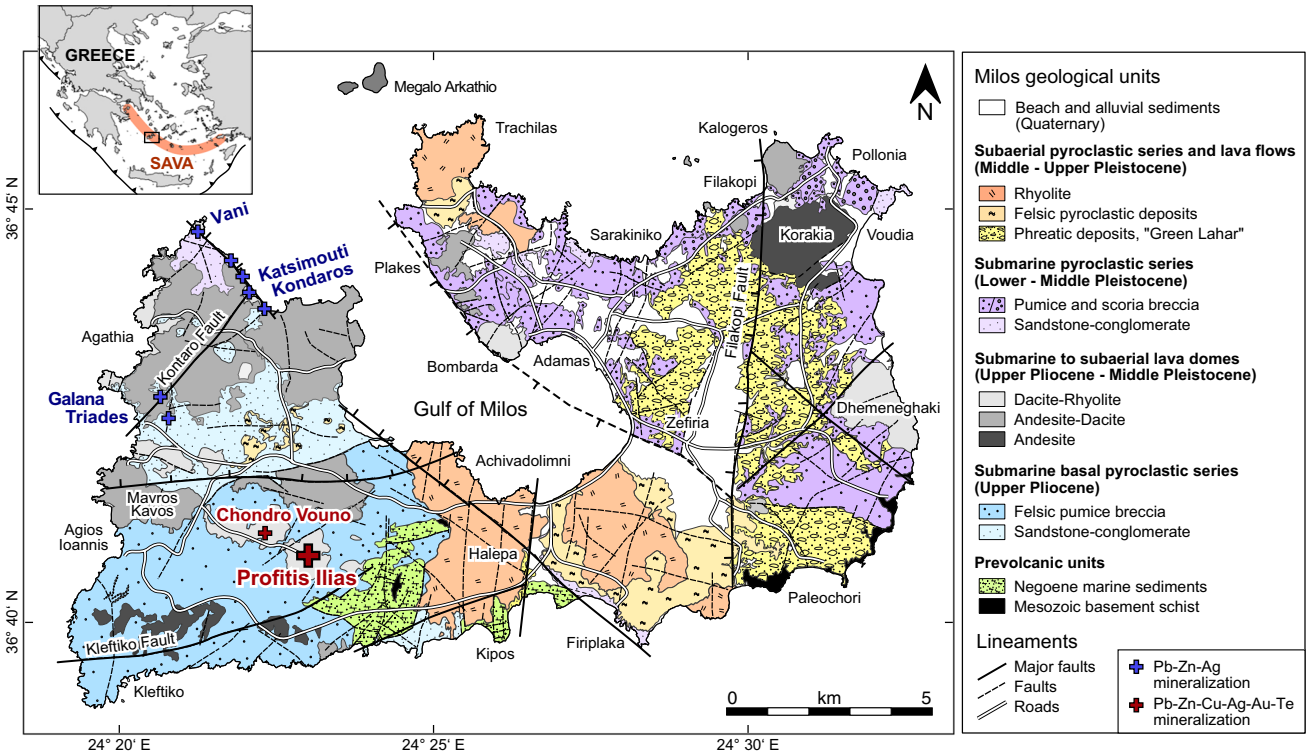

Fig. 1 Geological map of Milos (modified after Stewart and McPhie 2006; Schaarschmidt et al. 2021a) showing the locations of hydrothermal vein mineralizations. Profitis Ilias is the highest point of the island and hosts a Pb-Zn-Cu-Ag-Au vein mineralization. The inset shows the location of Milos in the South Aegean Volcanic Arc (SAVA)

and salinity (Kilias et al. 2001; Naden et al. 2003). Fluid inclusion thermometry indicates variable salinities of < 1 to 16 wt. % NaCl equivalent and decreasing minimum homogenization temperatures from ~ 250 °C to < 150 °C with increasing elevation (Fig. 2b; Kilias et al. 2001). Based on the homogeneous trapping of brines below 450 m and higher maximum homogenization temperatures above 450 m, Kilias et al. (2001) suggested the presence of a liquid-dominated zone below 450 m and a vapor-dominated zone above 450 m, generated by extensive boiling during fluid ascent (Fig. 2b). An upwards increasing vapor/liquid ratio of the hydrothermal system is supported by decreasing $\delta^{18}O$ values of quartz-hosted fluid inclusions (Fig. 2c; Naden et al. 2003). Gold and Ag concentrations in bulk ore samples show higher concentrations at shallow levels > 500 m (Fig. 2c) with a recorded maximum of 57 µg/g Au and 1200 µg/g Ag at 621 m (Naden et al. 2003). The observed Au enrichment is related to native Au and electrum in samples above 430 m (Kilias et al. 2001; Alfieris et al. 2013).

Samples and methods

During this study more than 100 segments from a total of 13 drill cores from Profitis Ilias were investigated that cover a depth range between 140 and 680 m elevation (ESM2, Tables S1, S2). Based on depth, alteration, and mineralization, 24 polished thin sections and 13 polished thick sections were prepared (Fig. 2d). Furthermore, ten polished sections from the same drill cores used in a previous study (Alfieris et al. 2013) and two polished sections from surface samples near the summit were included. Polished sections were studied by optical microscopy and unknown phases were identified by scanning electron microscopy (SEM) using a Hitachi TM 4000 equipped with an Oxford Instruments energy dispersive spectrometer (EDS) at the GeoZentrum Nordbayern, Friedrich-Alexander-Universität Erlangen-Nürnberg. The measurements were performed with an acceleration voltage of 15 kV.

Whole rock analysis

Representative samples were washed in an ultrasonic bath, crushed, milled to 50 µm in an agate mill, and were then dried at 55 °C for 24 h. For x-ray diffraction (XRD) analysis the samples were dried a second time at 105 °C for 12 h. The XRD analyses of the rock powders were performed by a Siemens D5000 diffractometer at the GeoZentrum Nordbayern (ESM2, Table S3). Mineral abundances (> 1 wt. %) were calculated using the Rietveld-algorithm with the Software Profex (Doebelin and Kleeberg 2015). The results are

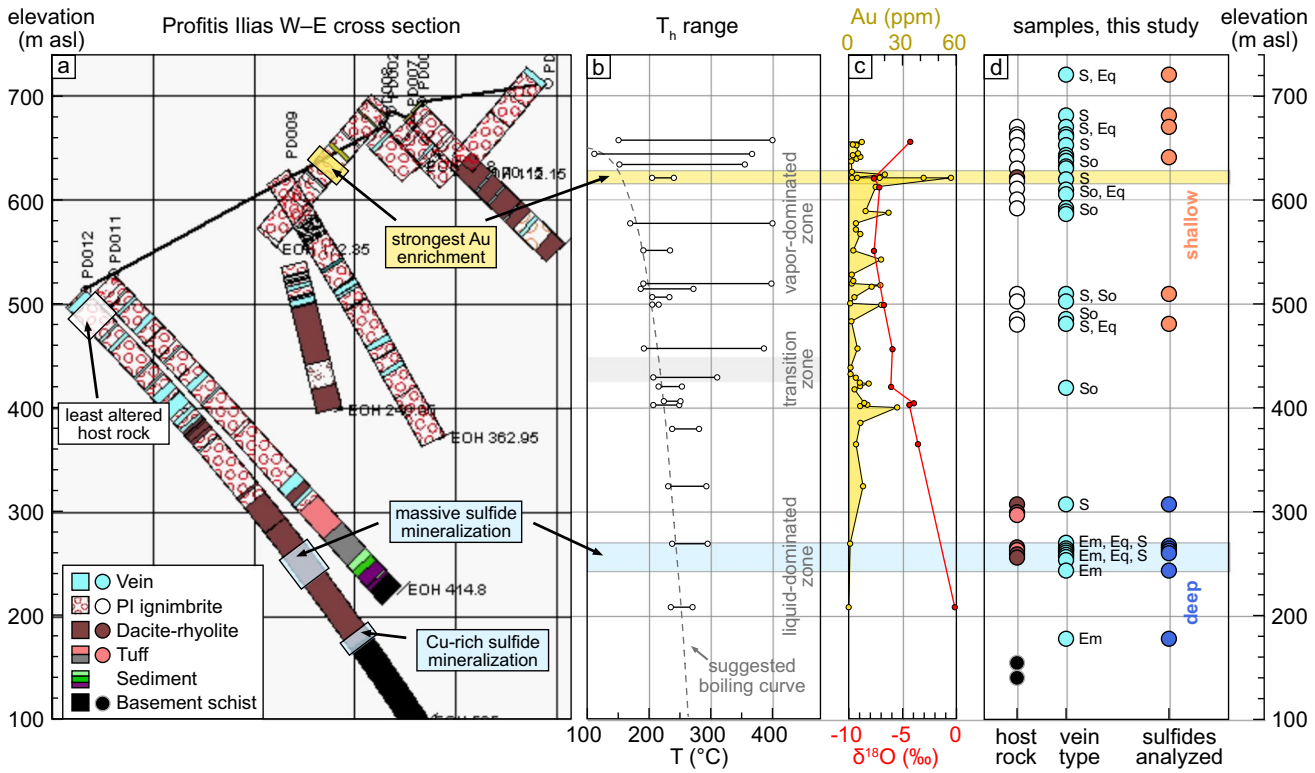

Fig. 2 (**a**) West–east cross section of the Profitis Ilias mountain with the geological profiles of selected drill cores (Alfieris 2006). The elevation is given in meters above sea level (m asl). (**b**) Range of homogenization temperatures of fluid inclusions in comparison with a boiling curve for a 5 wt. % NaCl equivalent fluid with 0.5 mol. % dissolved CO_2 (Kilias et al. 2001). (**c**) Bulk rock gold concentrations and $\delta^{18}O$ data of fluid inclusions (Naden et al. 2003). (**d**) Samples of host rocks, veins, and sulfides examined in this study. The uppermost two samples are surface samples; all other samples are from drill cores

semiquantitative since amorphous materials could not be quantified.

Whole rock samples with abundant sulfides were analyzed for major and trace elements at Activation Laboratories (Ontario, Canada) (ESM2, Table S4). The sample powder was fused using lithium meta- or tetraborate, followed by melting and then digestion of the molten sample in a nitric acid solution. Major element oxides and selected trace elements were analyzed using inductively-coupled plasma optical emission spectrometry (ICP-OES). Additional trace element analyses were performed by fusion inductively-coupled plasma mass spectrometry (ICP-MS). The measurements were calibrated and checked for quality by 14 certified USGS reference materials (ESM2, Table S5).

Sulfide-free whole-rock samples were analyzed for major element concentrations using a Spectro XEPOS He X-ray fluorescence (XRF) spectrometer, while trace element analyses were performed by a Thermo-Fisher Scientific X-Series 2 quadrupole ICP-MS at the GeoZentrum Nordbayern (ESM2, Table S4). For XRF analyses sample powders were processed to fused glass beads. Accuracy was monitored by measurements of the whole rock reference materials BE-N and GA (Govindaraju 1994); these results agreed with the assigned values to better than 7% for all major element oxides except for P_2O_5 (32%) (ESM2, Table S5). For ICP-MS trace element analyses sample powders were digested in HNO_3 and HF and processed following the method described in Schaarschmidt et al. (2021b). Accuracy was better than 13% for all reported trace elements, except for Sn which had a bias of 21%. The long-term reproducibility of the whole rock reference material BHVO-2 was better than 20% (2 s), except for Cs (40%). The elements Te, Re, and Au were measured on the same sample solutions following the other trace elements, as described in Regelous et al. (2020). Typical precision for Te, Re, and Au was between 1 and 5%, and reproducibility as determined by repeated analysis of a 10 pg/g standard solution was better than 7%.

Major and trace element analysis of sulfides

Twelve thick sections were investigated by electron microprobe analysis (EPMA) for the major and minor element composition of sulfides and other metal-bearing phases (e.g., tellurides) using a JEOL JXA-8200 Superprobe at the GeoZentrum Nordbayern. Spot analyses of mineral cores and rims were performed. The elements S, Fe, Pb, Zn,

Cu, Sb, As, Cd, Ag, Au, and Te were determined (ESM2, Table S6). All analyses were performed with a focused beam using an acceleration voltage of 20 kV and a beam current of 20 nA. The detection limits during EPMA were below 0.03 wt. % for all elements. Only major element concentrations > 0.1 wt. % were considered for the data interpretation; for trace element concentrations < 0.1 wt. % LA-ICP-MS data were used.

Fourteen sections from different elevations were analyzed for their trace element compositions in pyrite, sphalerite, galena, and chalcopyrite using laser ablation (LA-)ICP-MS at the GeoZentrum Nordbayern (ESM2, Table S7). More than 300 spot analysis of mineral cores and rims were performed. An Analyte Excite 193 nm laser from Teledyne Photon Machines coupled with an Agilent 7500c ICP-MS operated with a plasma power of 1280 W. Helium (0.9 l/min) and argon (0.94 l/min) were used as carrier gases. Argon (14.9 l/min) was used as both the plasma gas and auxiliary gas (0.9 l/min). The external calibration of Mn, Fe, Co, Ni, Cu, Zn, Ga, Ge, As, Se, Mo, Ag, Cd, In, Sn, Sb, Te, Hg, Tl, Pb, and Bi was performed by the MASS-1 polymetal sulfide reference material (USGS). Gold was calibrated by the Po724 B2 SRM sulfide reference material (Memorial University, Newfoundland). A single spot ablation geometry with a 15 Hz repetition rate and a fluence of 3.06 J/cm^2 were used for the measurements at a beam diameter of 10 to 35 µm depending on the size of the analyzed grain. Background measurements of ~ 20 s were performed prior to ~ 22 s of sample ablation. The analytical uncertainty was monitored by the repeated analysis of the reference materials, which yielded 1 s repeatabilities between 5 and 12% for all elements (ESM2, Table S8). Additionally, reproducibility and accuracy were monitored by the repeated analyses of the UQAC-FeS-1 sulfide reference material (University of Quebec) (ESM2, Table S8). Elemental interference of ^{115}In with ^{115}Sn was corrected by the natural abundances for ^{115}In concentrations > 0.1 ng/g. Element concentrations, analytical uncertainties (1 sigma error), and minimum detection limits were calculated using GLITTER (Version 4.4.4, Macquarie Research Ltd., Sydney, Australia) (ESM2, Table S9). The minimum detection limits were 4 µg/g for Fe, 1 µg/g for Zn, between 1 and 0.01 µg/g for Mn, Ni, Cu, Ge, As, Se, Mo, Cd, Sn, Sb, Te, Hg and < 0.01 µg/g for Co, Ga, Ag, In, Au, Tl, Pb, and Bi.

Pb and S isotope analysis of sulfides

Five samples between 245 and 270 m elevation were chosen for lead isotope ratio analysis due to the large grain size and dominant occurrence of sphalerite in this interval that allows for simple mineral separation. Pure sphalerite grains were handpicked and analyzed following Schaarschmidt et al. (2021a). Lead isotope analyses were performed by a Thermo-Fisher Neptune multi-collector (MC) ICP-MS at the GeoZentrum Nordbayern, using a ^{207}Pb/^{204}Pb double spike to correct for instrumental mass fractionation. The internal uncertainty was less than 0.0003, 0.0003, and 0.0007 (2 s) for ^{206}Pb/^{204}Pb, ^{207}Pb/^{204}Pb, and ^{208}Pb/^{204}Pb. Repeated measurements of the NBS981 Pb isotope standard yielded ^{206}Pb/^{204}Pb, ^{207}Pb/^{204}Pb, and ^{208}Pb/^{204}Pb ratios of 16.9413 ± 0.0012, 15.4985 ± 0.0008, and 36.7209 ± 0.0024 (2 s, $n = 4$), respectively. All Pb data were normalized to values of 16.9410, 15.4993, and 36.7244 for the NBS981 Pb isotope reference material.

The in-situ δ^{34}S composition of selected spots ($n = 50$) in pyrite at ~ 10 µm spatial resolution were performed by secondary ion mass spectrometry (SIMS) at the GeoForschungsZentrum (GFZ) in Potsdam (ESM2, Table S10). Three polished sections from different elevations were gold-coated and analyzed using a Cameca 1280-HR SIMS instrument. The ^{34}S/^{32}S repeatability on the Balmat pyrite reference material was ± 0.1‰ (1 rsd) or better on all three days of data acquisition, corresponding to an uncertainty of the δ^{34}S values of ± 0.1‰ (1 s). The SIMS results were calibrated against a reference value of δ^{34}S = 15.1 for the Balmat pyrite (Crowe and Vaughan 1996). Further analytical details are presented in Schaarschmidt et al. (2021a). After SIMS analysis, the same spots were analyzed for their trace element composition by LA-ICP-MS following the procedure described above (ESM2, Table S7).

Results

Host rock mineralogy and geochemistry

The investigated host rock samples cover levels cut by cores between 141 and 670 m elevation and include samples of the Profitis Ilias ignimbrite, the dacitic lavas, the tuff units, and the basement schists (Fig. 2d). The volcanic host rocks show a porphyritic texture dominated by a microcrystalline to medium grained quartz-K-feldspar-sericite matrix with grain sizes generally between 5 and 50 µm (Fig. 3). The matrix of some shallow samples (> 500 m) also contains fine grained kaolinite or illite. The volcanic rocks contain euhedral tabular K-feldspar (Fig. 3a), which is partly altered to sericite (Fig. 3b-d). Some samples also contain sericitized plagioclase phenocrysts, anhedral quartz (Fig. 3c), and tabular chlorite crystals (Fig. 3b). Some samples contain reworked basement xenoliths (Fig. 3a) and volcanic rock fragments from deeper stratigraphic levels (Fig. 3b). The least altered samples are from the uppermost part of core PD12, where the matrix contains relict volcanic glass (Fig. 2a; Fig. 3a).

XRD analyses of ignimbrite, dacitic lavas, and tuff indicate mineral contents of ~ 30–50 wt. % quartz, ~ 30–60 wt. % adularia, and 0–12 wt. % sericite (ESM1, Fig. S1).

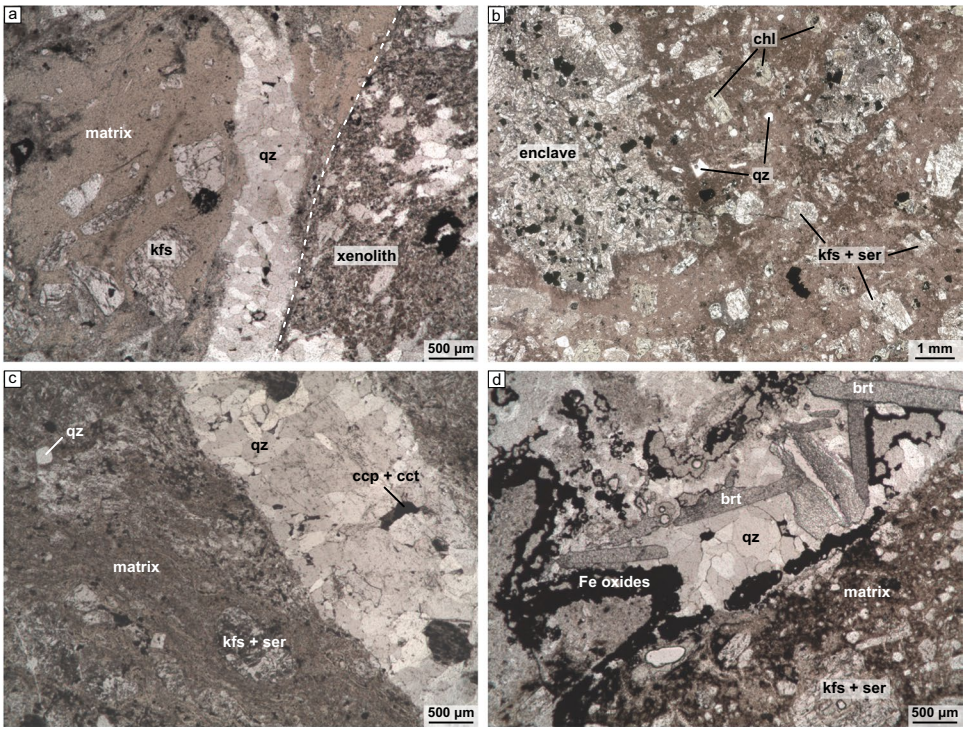

Fig. 3 Microphotographs of altered host rock at Profitis Ilias. Transmitted light, plane polarized. (**a**) Ignimbrite enclosing a metamorphic xenolith and crosscut by a quartz vein (S-type). The K-feldspar crystals are surrounded by a fine-grained matrix (PD12-14.6, 504 m elevation). (**b**) Altered dacite with sericitized K-feldspar, quartz, chlorite crystals, and volcanic enclaves (PD12-334.5, 255 m elevation). (**c**) Altered ignimbrite crosscut by a quartz-sulfide vein (Eq-type) (PD09-228.8, 479 m elevation). (**d**) Altered ignimbrite with vugs filled by quartz, barite, and Fe oxides or sulfates forming irregular overgrowth (PD05-91, 642 m elevation). brt = barite, cct = chalcocite, chl = chlorite, ccp = chalcopyrite, kfs = K-feldspar, qz = quartz, ser = sericite

Furthermore, some of the rocks contain up to 20 wt. % albite, 5 wt. % anorthite, 14 wt. % chlorite, 9 wt. % dickite, 11 wt. % illite, and 2 wt. % pyrite. About half of the analyzed rocks, especially the dacitic samples, have > 2 wt. % loss on ignition values, indicating the presence of significant amounts of hydrate and carbonate alteration phases. There is no systematic variation of the host rock mineralogy or geochemistry with elevation (ESM1, Fig. S1; ESM2, Tables S3, S4). The Profitis Ilias ignimbrite shows higher SiO_2 contents, lower MgO and Fe_2O_3 contents, and a larger variation of trace element compositions compared to the dacitic lava (Fig. 4a). The incompatible element composition of the volcanic host rocks (Fig. 4a) is enriched in Ba, K, and Pb, and is depleted in Cs, Nb, Ta, Sr, and P relative to upper continental crust (UCC; Taylor and McLennan 1985). The Profitis Ilias ignimbrite is enriched in Zn, Cd, Cu, As, Au, Ag, Sb, Te, and Pb, and depleted in Sn, Fe, Ni, and Co compared to UCC (Fig. 4b). The dacitic lavas are characterized by high concentrations in Zn, Cd, Te, Pb, and Tl.

The basement rocks consist of quartz (35 wt. %), albite (44 wt. %), muscovite (17 wt. %), and minor chlorite and pyrite. They show multiple cleavages, which are shaped by elongated muscovite grains and anhedral albite grains. Pyrite grains are anhedral to euhedral and lack deformation textures. The basement rocks show incompatible element characteristics similar to the volcanic rocks, but they have lower large ion lithophile element (LILE) contents and lack a positive Pb anomaly (Fig. 4a).

Vein mineralogy and geochemistry

At all elevations the altered host rocks at Profitis Ilias are cut by mm- to meter-thick veins. The mineralogy of the veins varies with the elevation. Four different epithermal vein types have been identified at Profitis Ilias: Silica-dominated (S-type) veins, silica-dominated oxide-bearing (So-type) veins, and two types of sulfide-bearing epithermal (Em- and Eq-type) veins (Table 1). The S- and E-type veins mutually crosscut each other (e.g., Fig. 5d).

The S-type veins consist mainly of quartz (> 90 vol. %), chalcedony, adularia, minor barite, small amounts of pyrite (< 5 vol. %) and other sulfides, such as galena and sphalerite (< 1 vol. %) (Figs. 3a and 5a). The grain size of euhedral, prismatic quartz crystals varies between 20 µm and several mm and often increases from the vein margin to the center. The S-type veins occur at all elevations, but are more abundant and thicker at higher elevations (> 600 m). Some S-type veins have brownish alteration halos.

A sub-group of silica-dominated veins has associated oxides (> 5 vol. %), barite, and minor pyrite (So-type veins; Figs. 3d and 5b). These contain goethite, hematite, anatase, Mn-, and Pb-oxides, as well as metal sulfates or carbonates, such as jarosite and malachite. Large barite crystals occur in the center of this vein-type and oxides form crusts that surround euhedral quartz and barite (Figs. 3d and 5b). This oxide-bearing assemblage occurs in veins, fractures, and cavities of the altered host rock at 10 to 100 m beneath

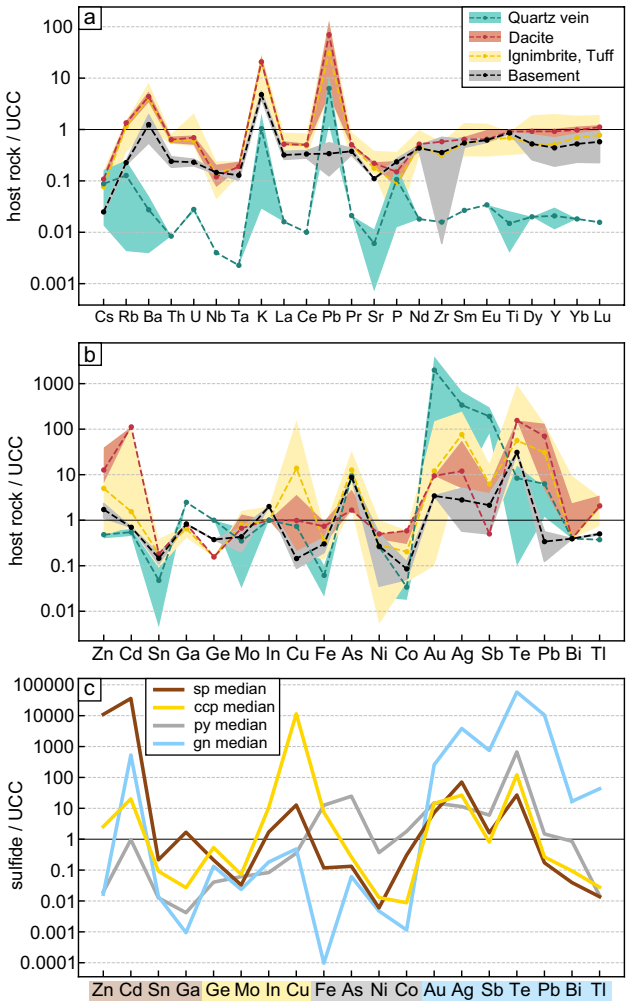

Fig. 4 Incompatible (**a**) and chalcophile (**b**) element concentrations of the host rocks relative to the upper continental crust (UCC; Taylor and McLennan 1985; Te content from Wedepohl 1995). Ranges and median compositions of the different host rock lithologies are shown. (**c**) Median chalcophile element concentrations of sulfides relative to the UCC. The elements are ordered by their main host sulfide phase. sp = sphalerite, ccp = chalcopyrite, py = pyrite, gn = galena

the surface (Table 1). The bulk rock geochemistry of two silica-dominated veins reveals SiO_2 contents > 90 wt. % and depleted incompatible trace element contents compared to the UCC (Fig. 4a). By contrast, one S-type vein at an elevation of 640 m shows strong enrichment of Au, Ag, and Sb together with low base metal and Te concentrations (Fig. 4b). This is in accordance with the occurrence of native Au or electrum (and Sb) in quartz veins as described by Kilias et al. (2001).

The Em-type veins include all veins that contain > 50 vol. % sulfides (mainly pyrite, sphalerite, chalcopyrite, and galena) and < 50 vol. % gangue minerals (Fig. 5c, d), whereas the Eq-type veins contain 5–50 vol. % sulfides (Fig. 3c). Subhedral to euhedral quartz is the main gangue phase in both the Em- and Eq-type veins. The Em-type veins range in thickness from 100 µm to several cm, they lack alteration halos, and have sharp boundaries to the host rock (Fig. 5d). The Eq-type veins merge with Em-type or S-type veins (Fig. 5d) and have the same textural features as the Em-type veins, but are generally thinner (< 5 mm). The Em-type veins occur only at elevations between 178 and 270 m where they are hosted by the altered dacite-rhyolite drilled in PD12. The main sulfides in both the Em- and Eq-type veins are pyrite, sphalerite, galena, and chalcopyrite in different proportions (Table 1; Fig. 6). Minor minerals include covellite, chalcocite-digenite, bornite, greenockite, tetrahedrite-tennantite, along with Ag(-Au)-tellurides. Alfieris et al. (2013) and Kilias et al. (2001) recorded native Au and electrum occurring as inclusions in base metal sulfides and in quartz.

Sulfide petrography

Pyrite is the most abundant sulfide mineral at the Profitis Ilias, and ubiquitous at all elevations. Four different pyrite types were identified according to textural differences and their relative occurrences in the mineral assemblage (Fig. 6). Pyrite 0 (py0) is disseminated in the altered host rock at all elevations (Fig. 7d). Inclusions and cavities are rare and the grain size of the subhedral to euhedral pyrites varies between 10 and 100 µm. The Em- and Eq-type veins both contain two types of pyrite (py1 and py2) that are associated with chalcopyrite, sphalerite, and galena (Fig. 7). Euhedral to subhedral pyrite 1 (py1) has a round, cubic, or hexagonal shape and varies in grain size from 20 to 1000 µm. Pyrite 1 also has a porous texture and commonly hosts inclusions of chalcopyrite, galena, sphalerite, and hessite (Fig. 7g-i). Pyrite 1 occurs along the margins of the Em- and Eq-type veins or as isolated grains in close proximity. Cracks commonly intersect py1 that are sealed by chalcopyrite, sphalerite, and covellite (Fig. 7l). Anhedral to euhedral pyrite 2 (py2) has a grain size of 20 to 400 µm, and is less porous and hosts fewer inclusions than py1 (Fig. 7g, k). Pyrite 3 (py3) is associated with quartz, barite, and oxides in the So-type veins. It is anhedral and has a skeletal texture with grain sizes up to 500 µm (Fig. 7e).

Chalcopyrite exhibits a semi-massive texture and is typically associated with sphalerite, galena, and py1/2 (Fig. 7a-c, g, j-l). Chalcopyrite is most abundant in the deepest segment (178 m; Fig. 7k, l), but rare at high elevations, where it is surrounded by successive bornite, chalcocite-digenite, covellite, and galena (Fig. 7b, c, g, j).

Sphalerite occurs as large anhedral grains and is the dominant sulfide phase in the base metal zone between 178 and 270 m elevation, with modal amounts of 20–75 vol. % in the Em-type veins (Table 1). It mostly occurs together with chalcopyrite, galena, py1/2, and bornite-chalcocite-covellite (Fig. 7a, g, j-l). Sphalerite from the deepest part of the

Table 1 Occurrence of vein types with mineralogy. The relative abundance of sulfide minerals is given with M = minor (1–5%), C = common (5–25%), A = abundant (25–50%), and D = dominant (> 50%). Mineral abbreviations: adl = adularia, brt = barite, ccd = chalcedony, ccp = chalcopyrite, gn = galena, goe = goethite, gre = greenockite, hem = hematite, mlc = malachite, ox = oxide, py = pyrite, sp = sphalerite, tnt-ttr = tennantite-tetrahedrite. The Cu phase can include covellite, bornite, chalcocite and digenite

Sample	elevation (m)	vein type	thickness (cm)	gangue minerals	oxide minerals	py	sp	gn	ccp	Cu phase	trace (< 1%)
MI1817	721	Eq	4	ccd, qz			A	A			
MI1818	681	S	2	qz		C			M		
PD03-31,9	672	Eq	1.5	qz		C	A	M	M	A	tnt-ttr, gre
PD07-21,5	664	Eq	0.3	qz, adl, brt		C					
PD03-48	661	So	0.5	qz, brt							
PD08-21,7	656	So	2	qz, brt							
PD08-24	654	S	2	qz, ccd		M					
PD08-25	653	S	2	qz							
PD05-91	642	So	1	qz, brt	goe, hem	M					gre
PD06-8	640	So	> 5	brt, qz	Fe ox						
PD02-66	639	So	1	qz	Fe, Ti ox						
PD05-95	639	So	0.3	qz	Fe ox	M					
PD06-18	633	So	10	qz, adl, brt, mlc	Fe ox						
PD06-21,5	630	So	0.5	qz, brt	Fe ox						
PD03-104,4	621	S	1	qz		M					
PD03-104,65	621	S	0.8	qz							
PD04-48,5	611	Eq	0.3	qz		M	A	M	C	C	
PD03-118,8	611	So	0.8	qz, brt	Fe ox						
PD01-11,8	605	So	0.3	qz	Fe, Mn, Ti ox	M					
PD09-68	593	So	> 3	qz, ccd	Fe ox						
PD09-72	590	So	0.5	qz, ccd, brt	Fe ox						
PD09-73	589	So	0.5	qz, ccd, brt	Fe ox						
PD10-132	513	So	1	qz	Fe, Ti ox				M		
PD12-14	504	S	0.3	qz, mlc							
PD12-15,5	503	So	0.5	qz, adl	Fe ox						
PD12-38	486	So	0.1	-	Fe ox						
PD09-228,8	479	Eq	0.7	qz		C			C	C	tel
PD09-229,3	479	S	0.3	qz		M					
PD11-156	420	So	10	adl, clay	Fe ox	M					
PD11-317,2	306	S	0.5	qz		D					
PD12-315,3	270	Eq	0.5	qz		M	D	C	C	M	
PD12-315,3	270	Em	0.8	qz		M	D	C	C	M	
PD12-315,3	270	S	0.1	qz							
PD12-317,5	268	Em	> 10	-		C	D	C	M	M	gre
PD12-318,5	268	Em	> 5	-		C	D	M	C	M	tnt-ttr, tel
PD12-319	267	Em	0.5	-		C	D	C	M	A	gre, tel
PD12-319	267	S	0.2	qz							
PD12-320	266	Em	0.1	qz		A	M	C	A	C	tel
PD12-321	266	Em	0.1	qz		C	D			C	
PD12-321,25	265	Eq	0.3	qz		A	C		A		gre
PD12-322,5	264	Eq	0.2	qz		C	C	A	A		
PD12-322,5	264	S	0.3	qz							
PD12-322,85	264	Em	0.4	qz			C				
PD11-376,5	264	S	0.1	qz		M					
PD12-323,9	263	Em	0.8	-		C	A	C	M	M	
PD12-328,5	260	Eq	0.2	qz		C	A	A	M	M	
PD12-348	245	Em	0.5	qz		C	A	A	C	M	gre
PD12-433	178	Em	> 5	-		C	C	M	D	M	

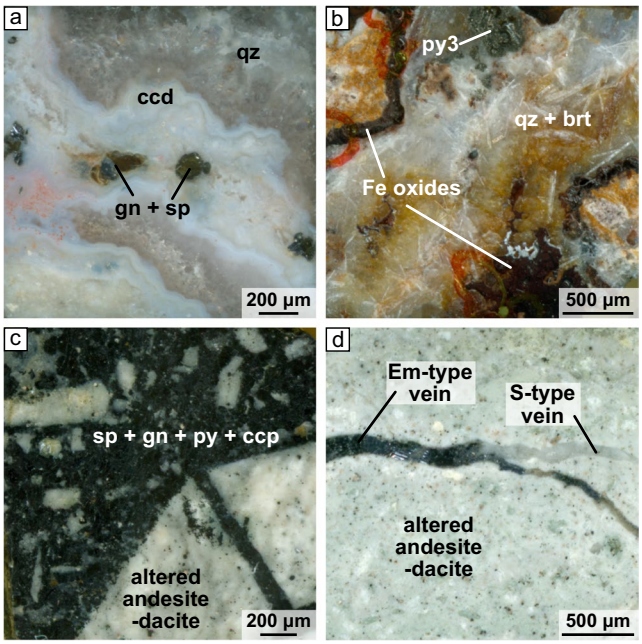

Fig. 5 Photographs of mineralized samples from Profitis Ilias. (**a**) Several cm thick Eq-type vein with quartz, chalcedony, and sulfides (MI1817, surface sample). (**b**) So-type vein with altered host rock fragments overgrown by goethite, quartz, and pyrite (PD05-91, 642 m elevation). (**c**) Thick Em-type vein with massive sulfides and brecciated host rock fragments (PD12-319, 267 m elevation). (**d**) Altered dacite crosscut by a sulfide (Em-type) vein that joins a quartz (S-type) vein (PD12-348, 245 m elevation). brt = barite, ccd = chalcedony, ccp = chalcopyrite, gn = galena, py = pyrite, qz = quartz, sp = sphalerite

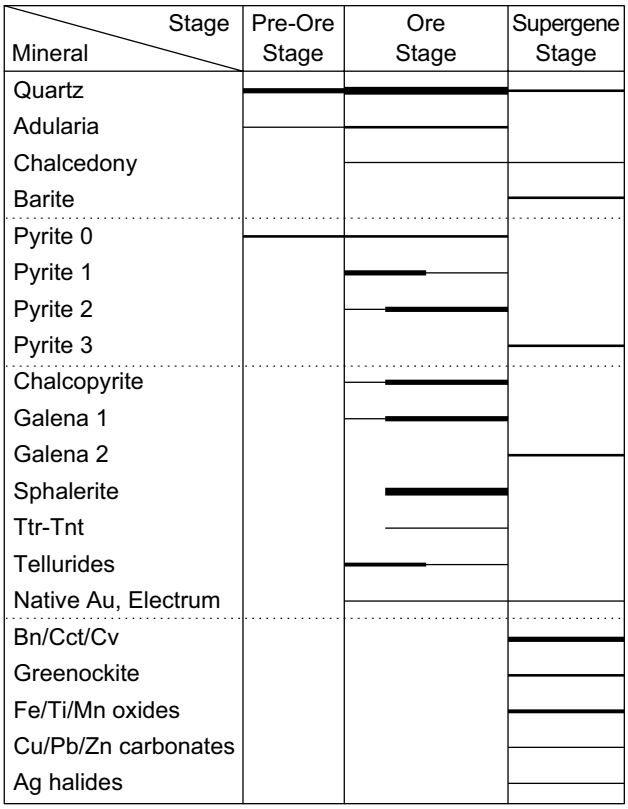

Fig. 6 Paragenetic sequence of the Profitis Ilias mineralization adapted from Kilias et al. (2001). The line width represents the relative abundance of the minerals in the different stages of ore formation

mineralization hosts chalcopyrite inclusions near the grain boundaries. The abundance of chalcopyrite inclusions in sphalerite decreases with increasing elevation, whereas the amount of bornite-chalcocite-covellite increases. In addition to chalcopyrite, inclusions of galena and minor tetrahedrite-tennantite, pyrite, and greenockite were identified (Fig. 7a).

Galena is a common sulfide at all elevations; two textural types were distinguished. Anhedral, semi-massive galena 1 (gn1) occurs together with sphalerite, chalcopyrite, and py1/2 (Fig. 7a, g, k) and it commonly hosts inclusions of chalcopyrite, pyrite, tetrahedrite-tennantite, and tellurides. Galena 2 (gn2) forms small, euhedral grains and is associated with bornite, chalcocite-digenite, covellite, and greenockite along the grain boundaries of chalcopyrite and sphalerite (Fig. 7j).

Minor tellurides occur as inclusions in py1 (Fig. 7h), gn1, and sphalerite at 267 m elevation within the most massive sulfide mineralization (Fig. 5c), whereas they are rare or absent at all other elevations. EPMA analyses identified hessite (Ag_2Te) as the main telluride phase (ESM2, Table S6) with rare petzite (Ag_3AuTe_2). High Au contents in the absence of Ag or Te were detected by EDS in micro-inclusions hosted by goethite surrounding euhedral quartz in some shallow So-type veins (Fig. 7f).

Sulfide chemistry

A wide range in trace element contents was observed between different sulfides and their sub-types, while contents also vary with elevation. The Au contents of pyrite, chalcopyrite, and galena overlap, but galena shows the highest median Au contents (Fig. 8a). Galena shows the highest contents of Ag, Te, Sb, Se, Tl, and Bi (Fig. 8b-e). Sphalerite is enriched in Ga, Ge, Mn, Sn, In, and Cd compared to the other sulfides (Fig. 8f), while chalcopyrite also has high In, Ge, and Sn, and the highest Mo concentrations. Pyrite is enriched in As, Co, and Ni compared to the other sulfides (Fig. 8g-h).

The gn2 associated with bornite-chalcocite-covellite was too fine grained for trace element analysis by LA-ICP-MS. Galena 1 shows increasing Ag, Sb, and Tl, but decreasing Te, Au, Se, Ge, and Bi concentrations from deep to shallow levels (Figs. 9a-b, 10a-b). The composition of galena displays a positive correlation of Ag and Sb ($R^2 = 0.72$) at a Sb/Ag mass ratio of ~ 1 (Fig. 10a). The Ag, Sb, and Au concentrations of galena from Profitis Ilias overlap with those from the other vein mineralizations in northwest Milos (Schaarschmidt et al. 2021a), whereas the

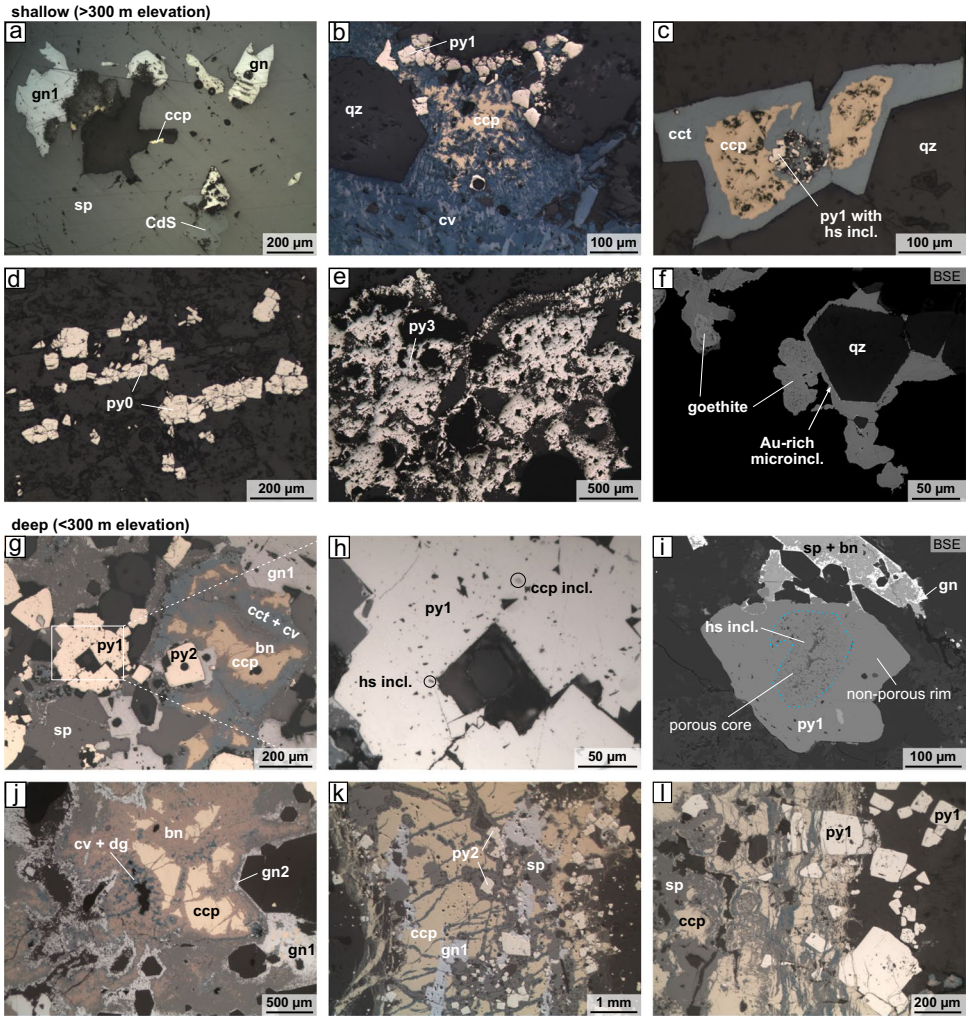

Fig. 7 Microphotographs of the sulfide mineralization at Profitis Ilias in the shallow (**a**-**f**) and deep (**g**-**l**) stockwork. Reflected light, except for two back-scattered electron (BSE) images (**f**, **i**). (**a**) Dominant sphalerite enclosing galena and minor chalcopyrite and being partly transformed to greenockite (CdS). (**b**) Subhedral pyrite (py1) associated with chalcopyrite that is almost completely replaced by covellite. (**c**) Pyrite and chalcopyrite surrounded by chalcocite in a quartz vein. (**d**) Disseminated pyrite (py0) within the altered host rock around the veins. (**e**) Large anhedral pyrite (py3) associated with barite and Fe oxides. (**f**) Vein quartz overgrown by goethite with Au-bearing microinclusions detected by SEM–EDX. (**g**) Typical sulfide assemblage at 267 m elevation consisting of porous and non-porous pyrite (py1 and py2), sphalerite, galena, and chalcopyrite surrounded by secondary Cu phases. Roundish holes are laser ablation craters. (**h**) Enlarged image of porous pyrite with inclusions of chalcopyrite and hessite. (**i**) BSE image of a zoned pyrite grain with a porous core (blue dashed line) and a non-porous overgrowth. The core has submicroscopic hessite inclusions. (**j**) Secondary transformation of chalcopyrite to bornite, covellite, digenite, and related fine grained galena (gn2). (**k**, **l**) Sulfide assemblage at 178 m elevation consisting of large porous pyrite (py1), followed by sphalerite, galena, non-porous pyrite (py2) and abundant chalcopyrite that is minorly replaced by covellite. bn = bornite, cct = chalcocite, ccp = chalcopyrite, cv = covellite, dg = digenite, gn = galena, hs = hessite, py = pyrite, qz = quartz, sp = sphalerite

Te concentrations in galena from Profitis Ilias are significantly higher (Fig. 10a-b). Sphalerite has variable Fe contents between 0.1 and 1 wt. % Fe (corresponding to 0.2 to 2 mol. % FeS) with a tendency toward lower Fe contents at higher elevations (Fig. 10d). Sphalerite shows increasing Ag and Sb concentrations, analogous to galena, and decreasing Co and Te concentrations with elevation (Fig. 9c, d). Sphalerite at Profitis Ilias generally has similar trace element content ranges, but higher Mn/Fe ratios > 0.1 (Fig. 10d) and higher Co concentrations up to 30 µg/g in the deep stockwork compared to the mineralizations of Kondaros-Vani and Triades on Milos Island (Fig. 10e; Schaarschmidt et al. 2021a). Trace element contents in chalcopyrite from Profitis Ilias show little variation with elevation, except for occasionally high As concentrations up to 2000 µg/g and lower Au/As and Sb/As ratios at low elevations (Fig. 10c).

The pyrite compositions at different elevations mostly overlap, but pyrite from shallower levels tends to show

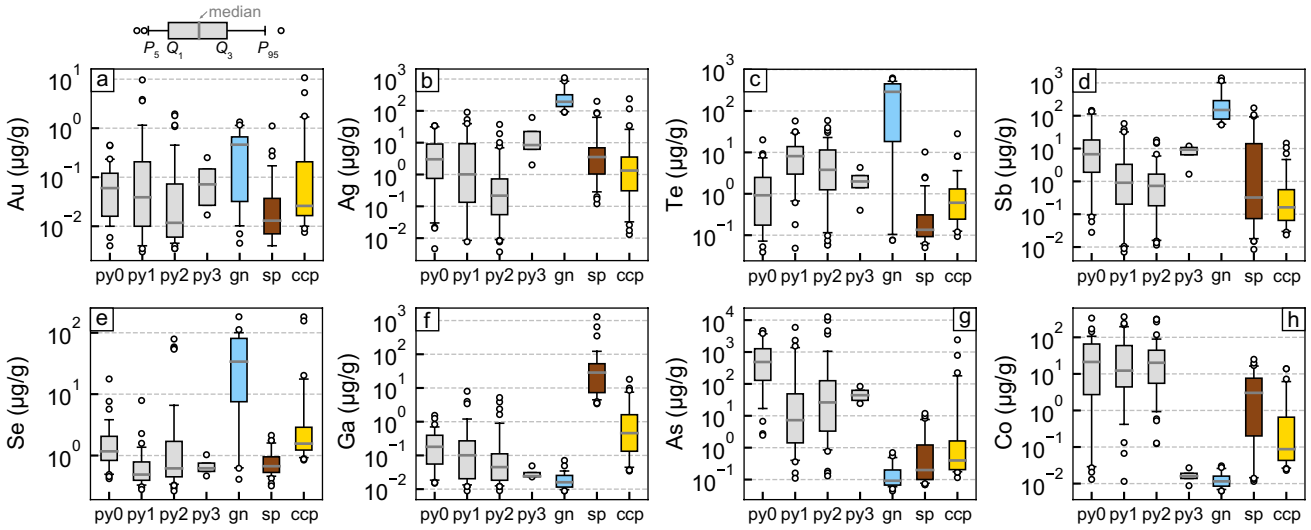

Fig. 8 Statistical trace element composition of pyrite (py0: $n=43$, py2: $n=48$, py1: $n=72$, py3: $n=4$), galena ($n=37$), sphalerite ($n=59$), and chalcopyrite ($n=54$) (ESM2, Table S7). Analyses with evidence for micro-inclusions are excluded. Analyses that lay below the minimum detection limit are included at half the detection limit

higher median Ag/Co (Fig. 9e) and Ag/Te ratios (Fig. 11a), as well as higher Tl concentrations (Fig. 11c). Some pyrite compositions reveal high Ag and Te concentrations > 100 µg/g, likely indicative of a combined ablation of pyrite and submicroscopic telluride inclusions (Fig. 11a; mineral inclusions marked with bold border). The Ag/Te ratio of ~ 1.7 indicates that these inclusions are dominated by hessite, but the inclusions are also partly enriched in Pb and Au (Fig. 11b, c).

The different pyrite generations (py0, py1, py2, py3) exhibit distinct trace element compositions as a function of sampling elevation (Fig. 11). Pyrite 1 and 2, which are both associated with chalcopyrite, sphalerite, and galena, overlap in their trace element composition (Fig. 8), and are, thus, not distinguished in Fig. 11. For the deeper drill core sections (< 300 m), the disseminated pyrite (py0) overlaps with the trace element composition of py1/2 (Fig. 11). By contrast, py0, py1/2, and py3 from the shallower part (> 300 m) show trace element compositions that are best distinguished based on the Tl/Pb ratio (Fig. 11c). The Tl/Pb, Tl/Cu, and Sb/Pb ratios increase from py1/2 to py0 to py3 (Fig. 11c, d). Pyrite 0 also has higher Co/Ni ratios than py1/2, while py3 has very low Co, Ni, Se, Sn, and Ge concentrations below the minimum detection limit (< 0.5 µg/g; Fig. 11e). Disseminated py0 has elevated Hg concentrations of up to 13 µg/g at 470 m elevation that correlate with increasing Tl/Pb ratios (Fig. 11f). The As concentration of pyrite varies from < 1 µg/g to 1.3 wt. %, but does not vary systematically with elevation or between pyrite generations (Fig. 11b). The trace element composition of pyrite from Profitis Ilias largely overlaps with that from the other Milos hydrothermal mineralizations (Fig. 11), with the exception of a Te enrichment at Profitis Ilias (Fig. 11a) and a depletion in Tl and Sb in pyrite from the deeper sections (Fig. 11c).

Sulfide Pb and S isotopic composition

The $^{206}Pb/^{204}Pb$, $^{207}Pb/^{204}Pb$, and $^{208}Pb/^{204}Pb$ ratios of sphalerite separates show a narrow range centered around 18.855, 15.688, and 39.001, respectively (Table 2; ESM1, Fig. S2). The Pb isotope ratios of sphalerites from Profitis Ilias lie within the range of published sulfide data from Kondaros-Katsimouti and Triades in northwest Milos (Schaarschmidt et al. 2021a). The Profitis Ilias sphalerite has slightly lower $^{207}Pb/^{204}Pb$ values (15.6875 to 15.6897 compared to > 15.6914 at Kondaros-Katsimouti-Triades), but this difference is within the external uncertainty (±0.003, ESM1, Fig. S2).

The $\delta^{34}S$ values of pyrite range from -0.1 to 5.3‰ (Fig. 9f; ESM2, Table S7). The sulfur isotope analyses comprise different elevations and different pyrite types. The median $\delta^{34}S$ values of each sample decreases with increasing elevation from 3.5‰ at 178 m to 2.4‰ at 681 m (Fig. 9f). The $\delta^{34}S$ values of the different pyrite types (py0 to py3) overlap and do not show any systematic trend.

Discussion

Metal(loid) budget of the Profitis Ilias mineralization

Metals in the Profitis Ilias mineralization are mostly concentrated in the sulfides in the Em- and Eq-type veins, but the altered volcanic host rocks also possess a significant

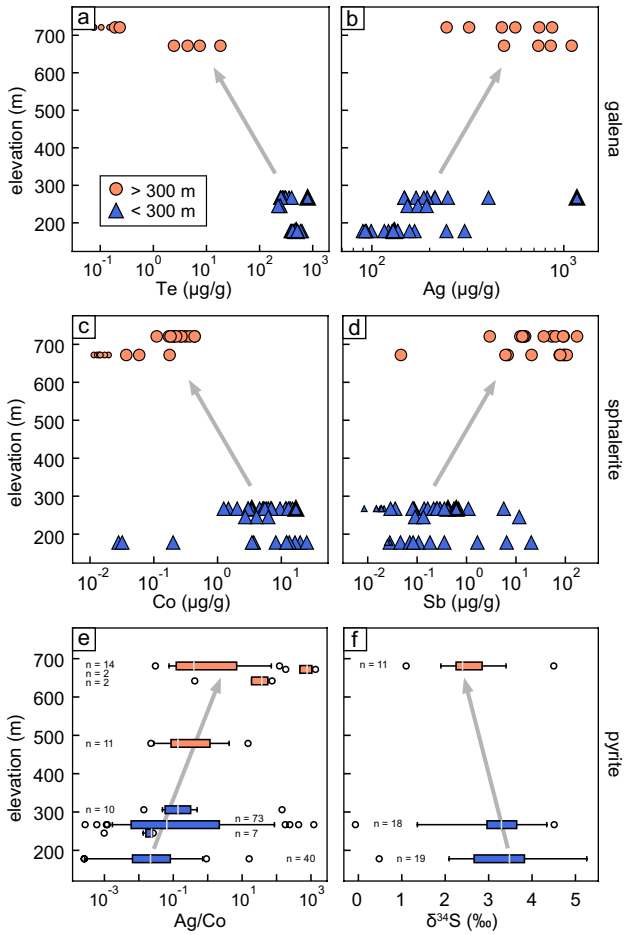

Fig. 9 Vertical geochemical variation of galena (**a**-**b**), sphalerite (**c**-**d**), and pyrite (**e**–**f**) at Profitis Ilias. (**a**-**d**) Analyses below the minimum detection limit are shown as small symbols at half the minimum detection limit. Analyses with evidence for detected micro-inclusions are marked with bold border. (**e**–**f**) Due to the high number of pyrite analyses, pyrite data is shown as boxplots for each elevation

enrichment of Zn, Cd, Cu, As, Au, Ag, Sb, Te, and Pb relative to UCC (Fig. 4b). The similar chalcophile element characteristics of the altered volcanic rocks and the sulfides (Fig. 4b, c) implies the presence of small sulfide veinlets and disseminated base metal sulfides. In order to quantify the element flux during hydrothermal alteration of the Profitis Ilias host rocks, the Ishikawa alteration index (AI) and the chlorite-carbonate-pyrite index (CCPI) were calculated (Ishikawa et al. 1976; Large et al. 2001). Both indices range between 60 and 98% for nearly all volcanic and volcaniclastic rocks; only two samples from high elevations (~ 500 m) have lower indices < 40% (weak to moderate alteration; Fig. 12a). The least altered sample (PD12-14.6) is located ~ 15 m beneath the surface and is most distal (> 200 m) to the central ore body. Dacite plots along the path of chlorite-pyrite alteration, whereas ignimbrite shows variable degrees of chloritic and sericitic alteration (Fig. 12a) in accordance with petrographic observations. There is no trend of the alteration indices with elevation. However, the presence of chlorite-sericite alteration with minor clays at depth and argillic alteration at the surface (Alfieris et al. 2013) is consistent with upwards decreasing fluid temperatures and a high water–rock ratio (White and Hedenquist 1990).

The composition of altered rocks relative to their unaltered precursors can be used to quantify the element flux during host rock alteration (Ague 2003; Mathieu 2018). In lieu of unaltered Profitis Ilias ignimbrite sample for comparison, we use two alternative references as unaltered rock compositions, (i) a dacitic lava from Mavros Kavos (MI1819; ESM2, Table S4) located 3 km northwest of Profitis Ilias (Fig. 1), and (ii) the least altered Profitis Ilias ignimbrite sample (PD12-14.6; Fig. 12a). The altered volcanic rocks from Profitis Ilias yield a general enrichment of Zn, As, Tl, Sn, and Pb and a weak depletion of Au, Ag, Cu, and Te relative to the least altered ignimbrite sample (Fig. 12b). However, the altered samples show a strong enrichment of Pb, Au, Ag, Cu, and Te relative to the unaltered Milos lava (Fig. 12b), which has only ~ 10 µg/g Pb and Cu and very low Ag, Au, and Te concentrations below the detection limit (< 0.08, < 0.002, < 0.001 µg/g, respectively; ESM2, Table S4). The metal concentrations of the least altered ignimbrite sample are, therefore, likely affected by some hydrothermal and/or supergene alteration and were initially lower, similar to the unaltered lavas. Trace element ratios of metals versus immobile elements such as Pb/Ti or Cu/Nb also show an increase by a factor of 30 to 70 from unaltered to altered rocks at relatively constant Ti and Nb concentrations (ESM2, Table S4). Thus, the uniform enrichment of As, Sb, Tl, Pb, Au, Ag, Cu, and Te during the alteration process suggests that these elements were enriched in the hydrothermal fluid and in the host rocks during fluid-rock interaction relative to the precursors.

The metamorphic basement schists show a weaker, but similar enrichment of As, Au, Ag, Sb, and Te relative to the UCC, whereas Pb and Cu are rather depleted (Fig. 4b). The absence of evidence for a primary enrichment of these elements in metasedimentary schists suggests a hydrothermal alteration overprint, in accordance with secondary mineral assemblages in basement rocks in the Zephiria graben in eastern Milos (Liakopoulos et al. 1991). The basement rocks at Profitis Ilias contain relatively high amounts of Na_2O (44% albite), low amounts of K_2O (no adularia), and minor amounts of disseminated pyrite (ESM1, Fig. S1), indicating only minor hydrothermal alteration. We suggest that this is related to a lower permeability of the schists relative to the overlying volcaniclastic and volcanic rocks. We further conclude that diffuse and focused flow of hydrothermal fluids caused the deposition of base metal sulfides, resulting in the observed enrichment of Zn, Cu, Pb, As, Au, Ag, Te, and Sb in both the altered host rocks and the veins. This also implies, that the

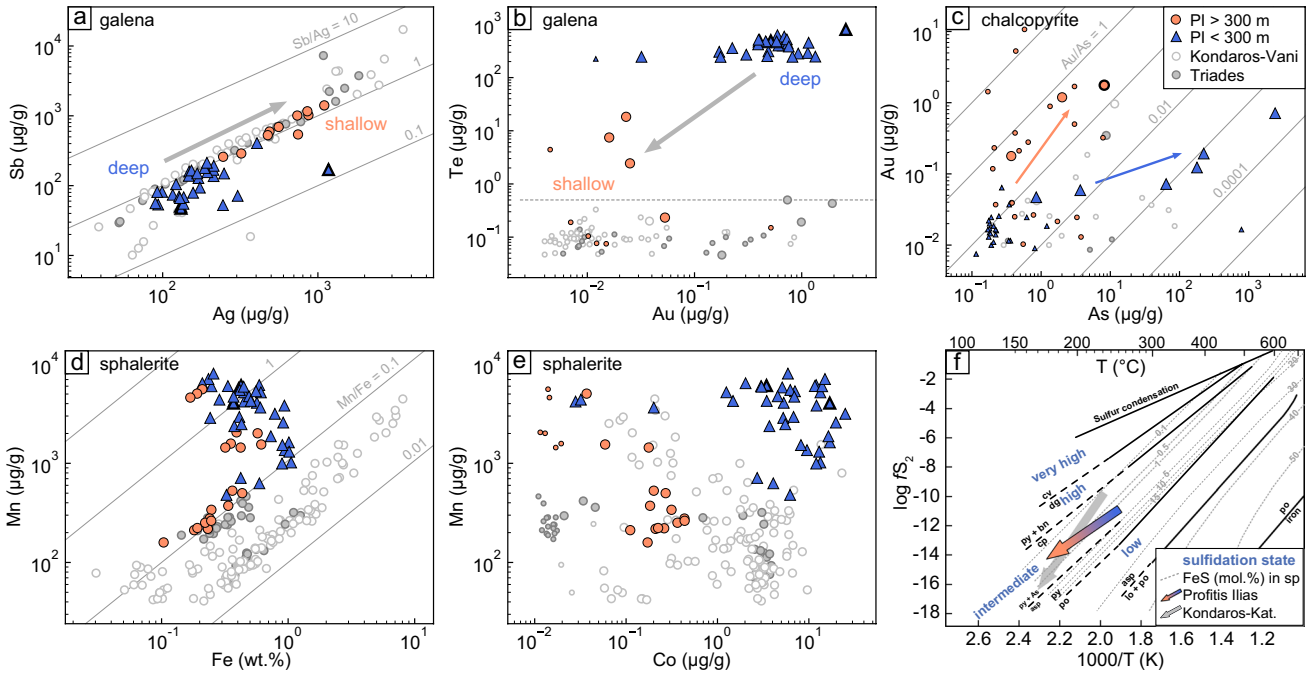

Fig. 10 (**a**-**e**) Major and trace element composition of sulfides from different elevations at Profitis Ilias. Sulfide composition data from mineralizations in northwest Milos are shown for comparison (Schaarschmidt et al. 2021a). Analyses that lay below the minimum detection limit are shown as small symbols at half the minimum detection limit. Analyses with evidence for micro-inclusions are marked with bold outline. (**a**-**b**) Galena from shallow levels has higher Ag and Sb, but lower Te and Au concentrations than galena from deep levels. (**c**) Chalcopyrite shows variable Au/As ratios at different elevations. (**d**-**e**) Sphalerite shows distinct Fe, Mn, and Co concentrations in different samples. (**f**) Estimated fluid evolution (temperature vs. sulfur fugacity) from deep to shallow levels at Profitis Ilias based on fluid inclusion temperatures (Kilias et al. 2001) and the FeS content in sphalerite (Scott 1983). The conditions at the Kondaros-Vani mineralization are taken from Schaarschmidt et al. (2021a)

metals concentrated in the veins were not mainly leached from the directly surrounding volcanic rocks; rather their source must be located below the deepest drill core section.

Metal and sulfur sources

The uniform Pb isotope ratios of galena and sphalerite from Profitis Ilias, Triades, and Kondaros-Katsimouti (Table 2; ESM1, Fig. S2; Schaarschmidt et al. 2021a) imply a uniform lead source for all hydrothermal systems over an area of > 30 km^2. Since the direction of hot fluid flow is upwards and the mineralization occurs near the contact to the basement metamorphic rocks, we expect that the metal enrichment of the fluid has been derived either through leaching of metamorphic and subvolcanic units beneath the drilled depth level or the input of magmatic volatiles that exsolved from a shallow intrusion at deeper levels. The metamorphic basement at Milos is heterogeneous in composition, ranging from mica schists to quartzites and gneisses (Liakopoulos et al. 1991). Lead isotope data of metamorphic basement rocks and volcanic rocks from Milos and neighboring islands exhibit a wide range, e.g., between 18.6 and 19.0 for $^{206}Pb/^{204}Pb$ (Schaarschmidt et al. 2021a; Stouraiti et al. 2017; Wind et al. 2020). Thus, local leaching of basement and subvolcanic rocks could have generated the observed Pb isotope composition of the sulfides. Although geochronological data suggest that the mineralizing events of western Milos occurred temporally unrelated to each other between 2.8 and 1.5 Ma (Miles 2021), the narrow range in the Pb isotope composition of sulfides (e.g. $^{206}Pb/^{204}Pb$ of 18.852 to 18.862) indicates, that Pb and perhaps other base metals were derived from a similar source. This can be explained by repeated fluid circulation through a large-scale fault network that crosscuts the basement and that was reactivated for focused fluid flow during the volcanic emergence of the island.

In contrast to Profitis Ilias, tellurides were not observed at Kondaros-Vani and Triades, and galena and pyrite have much lower Te contents, near or below the LA-ICP-MS detection limit (< 0.5 µg/g; Figs. 10b, 11a) (Schaarschmidt et al. 2021a). The distinct enrichment of Te at Profitis Ilias compared to the other Milos hydrothermal mineralizations (Figs. 10b, 11a) does not appear to be primarily controlled by specific fluid parameters, because the hydrothermal fluid temperature, fS_2, fO_2, and pH conditions (Fig. 10f) are similar at all locations (Naden et al. 2005; Alfieris et al. 2013; Smith et al. 2018; Schaarschmidt et al. 2021a). Tellurium has the highest gas–melt partition coefficient

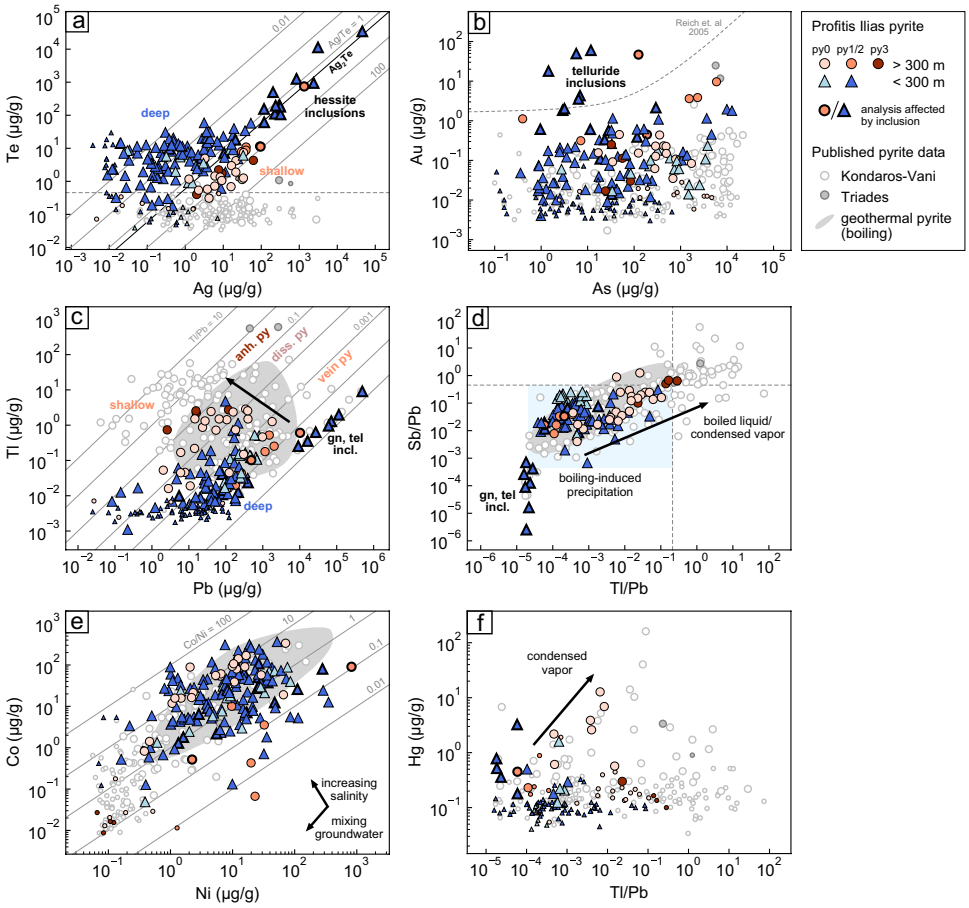

Fig. 11 Trace element composition of pyrites from different elevations and generations (py0, py1/2, py3) at Profitis Ilias. Analyses below the detection limit are shown as small symbols at half the detection limit. Analyses with evidence for micro-inclusions are marked with bold outline. Sulfide composition data from mineralizations in northwest Milos are shown for comparison (Schaarschmidt et al. 2021a). (**a**) The Ag/Te ratio in pyrite increases from deep to shallow levels. High Te and Ag concentrations at a Ag/Te ratio of ~ 1 represent mix analyses of pyrite and sub-microscopic telluride inclusions. (**b**) The As concentrations of all pyrite generations largely overlap. Some telluride inclusions also contain Au (Reich et al. 2005). (**c**-**d**) The Tl/Pb and Sb/Pb ratios in pyrite at high elevations increase from py1/2 (vein-type) to py0 (disseminated) and py3 (anhedral). The grey shaded field and the blue square displays the compositional range of pyrite that formed under boiling conditions (Román et al. 2019; Falkenberg et al. 2021). (**e**) Variable Co, Ni concentrations and Co/Ni ratios. (**f**) Some disseminated pyrites at 480 m elevation have elevated Hg concentrations that correlate with the Tl/Pb ratio

of all trace metals in volcanic systems (Zelenski et al. 2021) and is typically enriched in hydrothermal systems with an input of magmatic fluids (Berkenbosch et al. 2019; Kadel-Harder et al. 2020; Falkenberg et al. 2022). Therefore, we propose a model whereby the enrichment of Te at Profitis Ilias is due to an input of ascending volcanic gases exsolved from a shallow magma reservoir beneath Profitis Ilias.

Table 2 Lead isotope composition of sphalerite separates from Profitis Ilias

Sample	elevation (m)	$^{206}Pb/^{204}Pb$	$^{207}Pb/^{204}Pb$	$^{208}Pb/^{204}Pb$
PD12-315,3	270	18.8534	15.6885	39.0009
PD12-317,5	268	18.8600	15.6897	39.0045
PD12-318,5	267	18.8525	15.6882	39.0011
PD12-328,15	260	18.8515	15.6875	38.9984
PD12-348	245	18.8579	15.6875	39.0012

The in-situ $\delta^{34}S$ values of pyrite from Profitis Ilias (0 to + 5‰; Fig. 9f) overlap with previous S isotope data of sulfides from Milos (Marschik et al. 2010; Schaarschmidt et al. 2021a), though we found no negative $\delta^{34}S$ values as have been observed in pyrite at Kondaros-Katsimouti. Altogether, the S isotopes of sulfides from Milos neither exclude, nor support the input of magmatic S and can also be explained by thermochemical seawater sulfate reduction and leaching of S from host rocks (Shanks et al. 1981; Marini et al. 2011; Schaarschmidt et al. 2021a). A minor input of magmatic fluids at Profitis Ilias providing H_2S with potentially negative $\delta^{34}S$ values derived from disproportionation

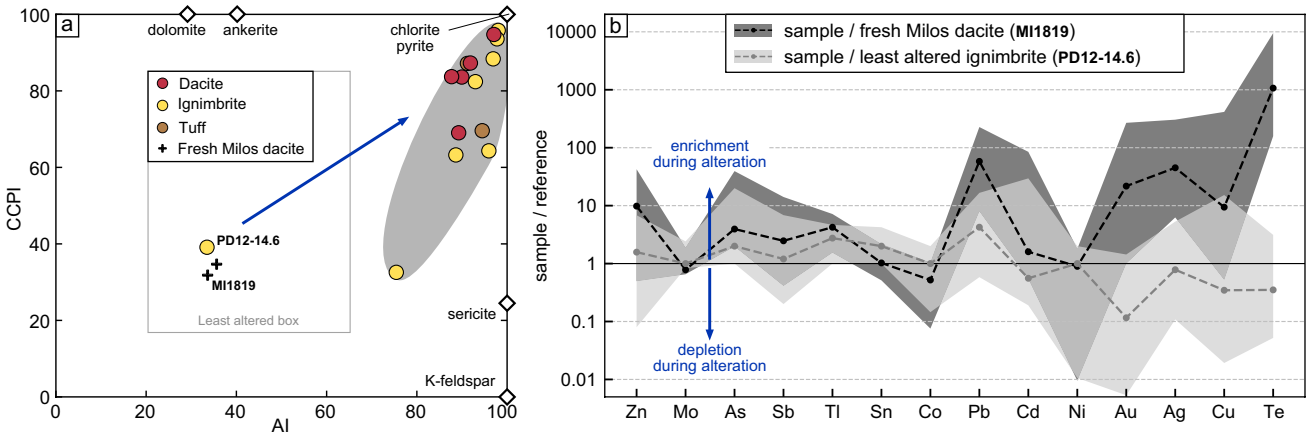

Fig. 12 (**a**) Ishikawa alteration index (AI) versus chlorite-carbonate-pyrite-index (CCPI) (Ishikawa et al. 1976; Large et al. 2001) of Profitis Ilias volcanic units and lavas from other locations at Milos Island. The unaltered lavas and one ignimbrite sample (PD12-14.6) plot inside the least altered box and are therefore used as precursor. The altered samples (grey field) display strong sericite-chlorite-pyrite alteration (blue arrow). (**b**) Multielement plot of the concentration of chalcophile elements (for hydrothermal environments) in the altered Profitis Ilias rocks relative to an unaltered Milos lava sample and relative to the least altered Profitis Ilias sample, respectively. Ranges of all samples and median values are shown. The elements are ordered from slightly chalcophile (left) to strongly chalcophile (right) (Barnes 2018)

of magmatic SO_2 (Herzig et al. 1998; Martin et al. 2020) could have been strongly diluted by H_2S with $\delta^{34}S$ values > 0 derived from the host rocks and from reduced seawater sulfate. This is in accordance with fluid $\delta^{18}O$ and δD values that indicate a dominance of seawater and a minor input of magmatic fluids in both the Milos fossil and active hydrothermal systems (Naden et al. 2005; Dotsika et al. 2009). We conclude that Te was likely introduced by volcanic gases that exsolved from a shallow magma chamber beneath Profitis Ilias, while most other metal(loids) are likely sourced from the metasedimentary basement.

Temporal and vertical evolution

Previous studies have shown that the evolution of the Profitis Ilias mineralization is divided into a hypogene stage and a later supergene oxidation stage (Kilias et al. 2001; Alfieris et al. 2013). An updated paragenetic sequence including our petrographic observations and interpretations is presented in Fig. 6. Both stages show vertical mineralogical and geochemical trends related to different fluid conditions and processes (Fig. 13) that will be discussed in the following.

Primary hydrothermal mineralization

The hypogene assemblage is characterized by early inclusion-rich pyrite (py1) followed by chalcopyrite, sphalerite, galena, and py2 (Fig. 7g-l). Inclusions of hessite and minor petzite, tetrahedrite-tennantite, and native gold occur as inclusions in pyrite (py1 and py2), galena, sphalerite, and chalcopyrite. Tellurides are only abundant in porous cores of py1 in the thickest (> 5 cm) Em-type veins at ~ 267 m elevation (Figs. 7g, h, 11a; ESM2, Table S6), but are absent below that level and only rarely occur at higher elevations (Fig. 7c). This suggests an abrupt change of the fluid conditions at ~ 267 m, most likely caused by vigorous boiling that triggered the co-precipitation of Te, Ag, Au, and base metal sulfides. The transition of Em-type veins at deeper levels to Eq-type veins above 300 m displays decreasing precipitation of base metal sulfides in accordance with decreasing base metal abundances caused by fluid boiling in a geothermal well (Clark and Williams-Jones 1990).

The alteration assemblage and gangue mineralogy is dominated by quartz, adularia, chalcedony, barite, sericite, pyrite (py0), and minor clay minerals, which suggests neutral pH values, typical for both low and intermediate sulfidation epithermal systems (Hedenquist et al. 2000). The high abundance of base metal sulfides and the Fe content of sphalerite (0.2 to 2 mol. % FeS) support an intermediate sulfidation state during the hypogene stage (Scott 1983; White and Hedenquist 1990) similar to the Kondaros-Vani mineralization (Alfieris et al. 2013; Schaarschmidt et al. 2021a). Slightly lower Fe concentrations in sphalerite at high elevations (Fig. 10d) suggest a slight increase within the intermediate sulfidation state from deeper to shallow levels during the hypogene stage (Scott 1983). Combined fluid inclusion thermobarometry (Kilias et al. 2001; Naden et al. 2003) and Fe contents of sphalerite suggest an evolution from log fS_2 = -11 at 250 °C in the deep stockwork to -14 at < 180 °C during fluid ascent (Fig. 10f). The decreasing log fS_2 values are in accordance with boiling of the

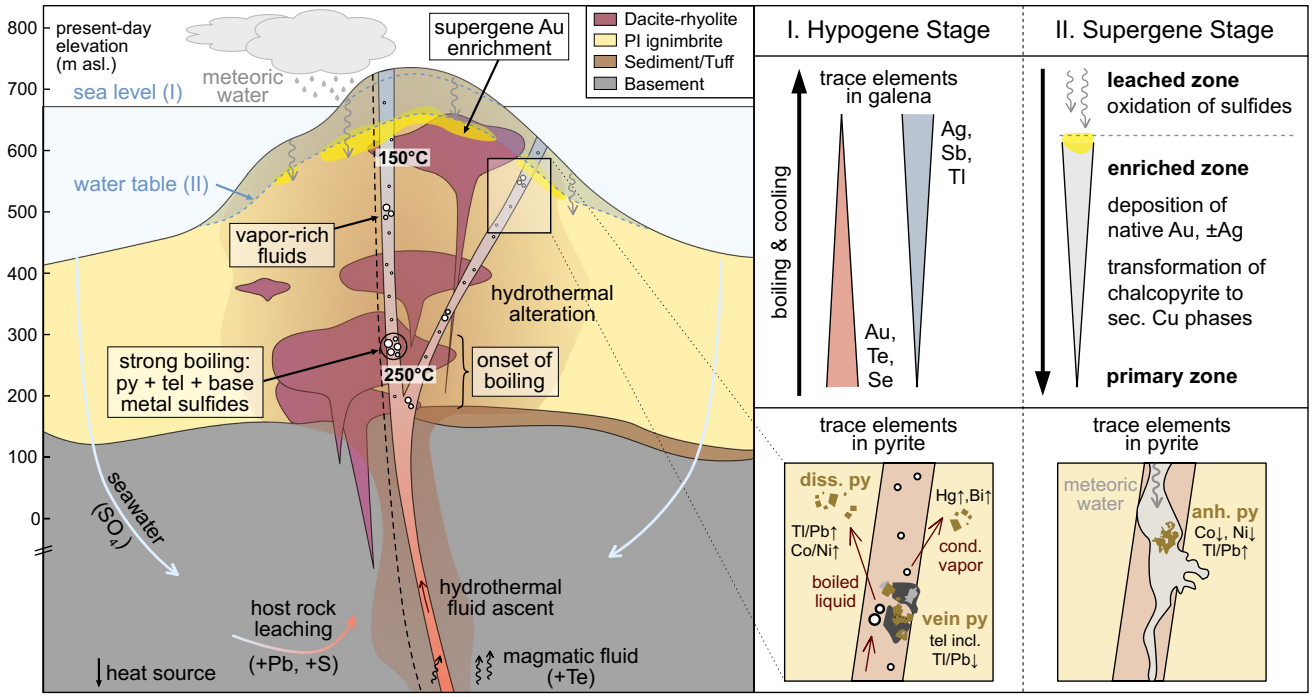

Fig. 13 Schematic profile of the Profitis Ilias mountain demonstrating the processes that controlled the formation of the mineralization during the hypogene stage (I) and the supergene stage (II) after exhumation to subaerial levels. The trace metal(loid) contents in galena show major vertical variations, whereas the trace element composition of pyrite show different characteristics for disseminated pyrite (py0), vein pyrite (py1/2) from the hypogene stage, and anhedral pyrite (py3) from the supergene stage (cf. Figure 6)

hydrothermal fluid and an increasing vapor/liquid ratio from deeper to shallow levels (Kilias et al. 2001; Naden et al. 2003) due to the transfer of H_2 and H_2S to the vapor phase (Reed and Spycher 1984; Cooke and McPhail 2001). Fluid boiling may also be responsible for the lower median $\delta^{34}S$ values with increasing elevation (Fig. 9f) due to the preferential oxidation of ^{34}S (McKibben and Eldridge 1990; Marini et al. 2011). A similar vertical trend to lower $\delta^{34}S$ values associated with fluid boiling was observed in a geothermal system in Central Mexico (González-Partida et al. 2005). The dominance of sulfides and absence of sulfates in the hypogene mineral assemblage indicate relatively reducing conditions and minor influx of seawater. The stability of hessite at 267 m elevation at ~ 250 °C suggests log fTe_2 values between -13 and -15 (Afifi et al. 1988; Plotinskaya et al. 2006).

Low Tl/Pb and Sb/Pb ratios of vein pyrite (py1/2) overlapping with published geothermal pyrite data (Fig. 11d; Román et al. 2019) support boiling-induced precipitation during the hypogene stage at all depth levels in accordance with textural observations. In the deep stockwork, the composition of vein pyrite (py1/2) and that of disseminated pyrite (py0) largely overlap (Fig. 11), suggesting that the hydrothermal fluid infiltrated the permeable host rock without causing any distinct geochemical changes. By contrast, in the shallow stockwork increasing Tl/Pb, Tl/Cu, Sb/Pb, and Co/Ni ratios (Fig. 11c-e) from vein pyrite (py1/2) to disseminated pyrite (py0) record the fluid evolution from fluid boiling in the veins towards a boiling-derived high-salinity fluid that infiltrated the host rocks. This is in accordance with published trace element data of pyrite that suggest elevated Tl/Pb and Tl/Cu ratios for boiled liquids relative to those ratios at the time of a boiling event (Simmons et al. 2016; Román et al. 2019; Falkenberg et al. 2021; Schaarschmidt et al. 2021a). Furthermore, high Co/Ni ratios in pyrite were shown to reflect high fluid salinities or temperatures due to the higher sensitivity of Co species to salinity and temperature changes (Brugger et al. 2016). High Hg and Bi concentrations in pyrite have been associated with vapor-rich fluids (Pokrovski et al. 2013; Simmons et al. 2016; Nestmeyer et al. 2021; Schaarschmidt et al. 2021a). The positive correlation between Hg (> 2 µg/g), Bi (> 2 µg/g), and Tl/Pb in several disseminated pyrite grains (py0) at 480 m elevation indicates a local enrichment of Hg and Bi by vapor condensation (Fig. 11f). This is in agreement with the occurrence of low-salinity, vapor-rich fluid inclusions at the same elevation (Kilias et al. 2001). We propose that a combined increase in Hg and Bi concentrations in pyrite documents vapor condensation above a local boiling zone, while elevated Tl/Pb ratios apply for both the boiled liquid and condensed vapor fluids.

Based on the boiling curve of the hydrothermal fluid (Fig. 2b; Kilias et al. 2001) the sea level at the time of

hydrothermal activity was located at present-day elevations between ~ 650 and 700 m (Fig. 13). There is no evidence for extensive acid-induced alteration caused by vapor condensation above zones of fluid boiling in the exposed depth levels at Profitis Ilias. However, boiled-off gases may have generated the argillic alteration near the summit (White and Hedenquist 1990). Besides the decreasing temperature, fS_2, and the variable fluid salinities (Kilias et al. 2001), which are all related to isenthalpic fluid boiling (Cooke and McPhail 2001), a strong vertical variation of pH or fO_2 in the fluid chemistry during the hypogene stage is absent in accordance with the monotonous alteration assemblage. However, there is evidence for local fluctuations of the sulfidation state, redox conditions, and metal supply during sulfide precipitation, such as Fe zoning within large grains of sphalerite or element and textural zoning in py1 (Fig. 7i).

Supergene mineralization and secondary Au enrichment

During a supergene mineralization stage (Fig. 6) chalcopyrite from the hypogene stage was successively transformed to bornite, chalcocite, digenite, and covellite (Fig. 7b, c, g, j), while sphalerite was partly transformed to greenockite (CdS; Fig. 7a). In contrast to Kilias et al. (2001), we suggest that bornite formed as a secondary mineral during the supergene stage. This is supported by the texture of bornite and other Cu sulfides, which surround and replace chalcopyrite along cracks and grain boundaries (Fig. 7g, j) up to a complete replacement by secondary Cu sulfides (Fig. 7b). The abundance of secondary Cu sulfides relative to primary chalcopyrite increases with increasing elevation where the least overprinted chalcopyrite-dominated mineralization was found at 178 m elevation (Fig. 7). This mineral transformation is typical for weathered sulfide deposits and records the downward migration of supergene Cu-rich fluids into the reducing environment below the paleo-water table (Sillitoe 2005; Guilbert and Park 2007). At the same time, the occurrence of goethite, hematite, Mn and Ti oxides, jarosite, barite, and Cu-Pb-Zn carbonates in the near-surface sections (uppermost 20 to 100 m, Table 1; Kilias et al. 2001) is typical for the leached zone of weathered sulfide deposits due to the infiltration of oxidizing meteoric water above the paleo-water table (Sillitoe 2005; Guilbert and Park 2007). Pseudomorphs of Fe oxides replacing euhedral disseminated pyrite record the oxidation of Fe^{2+} and dissolution of S by neutral pH meteoric waters (Butt 1998). Thus, the primary hydrothermal mineralization was overprinted by supergene processes at Profitis Ilias, generating a secondary vertical zonation that can be divided into the leached zone above the paleo-water table and the enriched zone below the paleo-water table, transitioning downwards into the hypogene mineral assemblage (Fig. 13). The occurrence of anhedral pyrite (py3) associated with supergene Fe oxides at 642 m (Fig. 5b) indicates fluctuating redox conditions. The secondary Cu sulfides are partly accompanied by fine grained galena (gn2), suggesting minor dissolution and reprecipitation of galena during the supergene stage. Sharp decreases in the Co, Ni, Ge, In, and Sn contents in py3 compared to hypogene py (Fig. 11e) support precipitation from cold, metal-poor meteoric water during the supergene stage. However, relatively high contents of Au, Ag, and Sb in py3 (Fig. 8) record remobilization of precious and semi-precious metals by supergene fluids.

The occurrence of native Au, electrum, and silver halides at Profitis Ilias in association with supergene goethite (Fig. 7f), covellite, and Cu oxides indicates a supergene enrichment of gold at > 400 m elevation. The dissolution and reprecipitation of Au and Ag is a common feature of weathered porphyry, epithermal, or massive sulfide deposits with a supergene enrichment of Au and Ag around the paleo-water table (Butt 1998; Milési et al. 1999; Páez et al. 2016; DeMatties 2018). Similarly to Profitis Ilias, the leached zone in such environments is characterized by silver halides and native Au, while the enriched zone exhibits coarse grains or nuggets of native Au and electrum (Milési et al. 1999; Guilbert and Park 2007; Páez et al. 2016; Arfè et al. 2016). The extensive supergene mineralization at Profitis Ilias requires tectonic uplift of several hundred meters to subaerial levels, in accordance with the volcano-tectonic evolution of the island (Stewart and McPhie 2006; Zhou et al. 2021). The maximum bulk rock Au concentrations are recorded at 610 to 640 m elevation (this study; Kilias et al. 2001) suggesting that the water table was located around that level during the supergene stage (Fig. 13). We conclude that the shallow Au enrichment at Profitis Ilias was enhanced by supergene processes and that it is not due to fluid boiling during the hypogene stage, which on the contrary caused decreasing Au and Te contents from deep to shallow levels (Fig. 10b).

Transport and deposition of Te, Au, Ag, and trace metal(loid)s

The vertical distribution of metal(loid)s in the hypogene base metal sulfide-telluride assemblage provides insight into the transport and precipitation processes that were active during fluid ascent. Both the cooling and boiling of the hydrothermal fluid, as indicated by fluid inclusion and stable isotope data (Fig. 2b, c) may affect the metal fractionation and deposition during fluid ascent (Reed and Palandri 2006; Simmons et al. 2016; Grant et al. 2020; Falkenberg et al. 2021; Schaarschmidt et al. 2021a). The decreasing Te, Au, Se, Bi, and Co and increasing Ag, Sb, and Tl concentrations in galena and sphalerite with increasing elevation (Figs. 9, 10) record the contrasting behavior of the two groups of elements during fluid flow from deeper to shallow levels (Fig. 13). Pyrite provides a similar, more continuous vertical trend towards increasing Ag/Te and Ag/Co ratios from 180 to 720 m elevation (Figs. 9e, 11a). Trace element systematics of hydrothermal

pyrite and bulk ore show that high Tl and Sb contents are related to lower fluid temperatures, whereas Se, Bi, and Co are typically enriched at higher fluid temperatures (Huston et al. 1995; Schmidt et al. 2007; Maslennikov et al. 2009; Keith et al. 2018b; Wind et al. 2020), which is in accordance with the element distribution at Profitis Ilias. Experimental and natural data suggest that the precipitation of Te and Au is not primarily affected by temperature changes, but is strongly controlled by H_2S loss and redox changes during processes like fluid boiling or fluid-rock interaction (Drummond and Ohmoto 1985; Clark and Williams-Jones 1990; Grundler et al. 2013; Keith et al. 2018b, 2020). This is in accordance with high Te and Au contents in galena at deeper levels, where sulfide precipitation is triggered by boiling. By contrast, Sb and Tl are less sensitive to boiling and either remain in the liquid or partition into the vapor phase, resulting in the enrichment of Sb and Tl at shallow levels above zones of fluid boiling (Simmons et al. 2016; Román et al. 2019; Nestmeyer et al. 2021). Silver is expected to precipitate during fluid boiling due to the destabilization of metal complexes triggered by vapor phase extraction, similar to the behavior of Au, Te, Cu, and Pb (Seward et al. 2014; Simmons et al. 2016). This indicates that the localized precipitation of Ag(-Au) tellurides at 267 m followed by massive base metal sulfides is related to fluid boiling. In contrast the upwards increasing Ag/Au ratios of galena imply a different behavior of the two precious metals during fluid ascent. We conclude that the solubility of Ag remains relatively high at ~ 250 °C, only decreasing at lower temperature or with increasing pH induced by vigorous boiling.

Similar increases in the Ag, Sb, and Tl concentrations of sulfides towards the upper part of the boiling zone have been reported from the Kondaros-Vani mineralization in northwest Milos (Schaarschmidt et al. 2021a). Those authors predicted higher Co, Ni, and Se concentrations at deeper levels, analogous to vertical trends observed in geothermal wells in New Zealand (Simmons et al. 2016) and Iceland (Grant et al. 2020). This is confirmed by generally higher Co and Ni contents (1 to > 100 µg/g) in pyrite (Fig. 11e) and higher Se contents (> 20 µg/g) in galena from the deep stockwork at Profitis Ilias. Galena from the shallow stockwork shows lower Se and Au concentrations that overlap with galena from Kondaros-Vani (Fig. 10b), which confirms that the shallow veins of the Profitis Ilias mineralization resemble the Kondaros-Vani system. Thus, we conclude that the vertical trends of metal(loid) concentrations in sulfides at Profitis Ilias are related to combined cooling and boiling of the hydrothermal fluid during ascent.

The initial mineral deposition during the hypogene stage at 267 m is recorded by porous, inclusion-rich cores of py1 (Fig. 7h, i) that formed during rapid crystallization triggered by vigorous fluid boiling (Román et al. 2019; Börner et al. 2021). The non-porous, euhedral pyrite grains (py2) and py1 overgrowths (Fig. 7g-i) record a shift towards more stable fluid conditions during mineral growth with less mineral inclusions. Nonetheless, rare telluride inclusions in py2, galena, sphalerite, and chalcopyrite imply that Te oversaturation persisted after the initial boiling event. We conclude, that the pressure release during the ascent of a ~ 250 °C hydrothermal fluid along subvertical fractures caused vigorous boiling at ~ 270 m elevation, triggering the abrupt precipitation of pyrite, Ag(-Au)-tellurides, and native Au, followed by base metal sulfides (Fig. 13). This is in accordance with the fluid model suggested by Kilias et al. (2001) and points out, how fluid boiling directly influences the vertical distribution of major and trace metals in hydrothermal systems. Consequently, sulfide precipitation in the E-type veins at levels below 270 m was apparently triggered by gentle boiling and/or a more gradual cooling that did not provoke the deposition of tellurides. A partitioning of Te into the vapor phase during boiling, as has been reported at moderately reducing conditions in neutral pH fluids (Grundler et al. 2013; Keith et al. 2020), is not observed at Profitis Ilias. There is no Te enrichment at high elevations, where the vapor/liquid ratio would have been higher and where the vapor would have condensed into the groundwater. The similar behavior of Te and Au during fluid boiling and cooling at Profitis Ilias implies that the physicochemical conditions promoted co-precipitation of Te and Au rather than a decoupling of the two elements.

Conclusions

The petrographic and geochemical study of drill core samples down to 550 m depth transecting the Profitis Ilias Pb-Zn-Cu-Ag-Au mineralization generally supports and refines the existing genetical models by Alfieris et al. (2013), Kilias et al. (2001), and Naden et al. (2005). However, most importantly it provides a detailed understanding of the processes that control the vertical distribution of metals and metalloids in shallow-crustal hydrothermal systems. The mineralogy and geochemistry of the host rocks reveal intense hydrothermal alteration dominated by chlorite, pyrite, sericite, adularia, and minor clay minerals that is most intense in the central part of the mineralization and decreases distal to the mineralization (Fig. 13). A comparison of the metal contents of altered Profitis Ilias volcanic rocks and unaltered lavas from Milos suggests an enrichment of most chalcophile elements, in particular Zn, Pb, Cu, Au, Ag, and Te, during fluid circulation and fluid-rock interaction. Uniform Pb isotope ratios of sulfides point towards a common metal source in the basement rocks beneath western Milos that was repeatedly leached during the volcanic emergence of the island. The enrichment of Te in sulfides and the presence of tellurides at Profitis Ilias is distinct, indicating the addition of Te

from volcanic gases to Profitis Ilias which, in turn, requires a shallow magma chamber beneath southwest Milos. We cannot exclude that this magmatic fluid also provided other elements such as As, Se, or Bi to the hydrothermal system, however, in contrast to Te, the concentration of these elements shows little variation in the shallow parts of all vein systems in western Milos.

The formation of the Profitis Ilias mineralization and the deposition of metals and metalloids was affected by (i) the ascent of a 250 to 150 °C, metal-rich hydrothermal fluid along subvertical faults and fractures and (ii) the downwards migration of oxidized meteoric water through open veins (Fig. 13). Fluid cooling and boiling during ascent of the hydrothermal fluid triggered base metal sulfide precipitation and caused a distinct vertical distribution of metal(loid)s. We observe an increase of Ag, Sb, and Tl and a decrease of Au, Te, Se, Bi, and Co concentrations in the sulfides from deeper to shallow levels (Fig. 13), which are related to decreasing fluid temperatures and to fluid boiling. This model resolving the vertical distribution of metal(loid)s may be transferred to the upflow zones of other epithermal, geothermal, or shallow submarine hydrothermal systems, where boiling of relatively low-temperature (< 300 °C) fluids controls the deposition of ore minerals.

Different pyrite generations record the fluid evolution from the onset of vigorous boiling (low Tl/Pb ratios, porous textures, Ag(-Au)-telluride inclusions) towards a boiled, high-salinity fluid (higher Tl/Pb, Co/Ni ratios) infiltrating the host rocks. The local occurrence of Hg- and Bi-rich pyrite reflects precipitation from vapor-rich fluids above local boiling horizons. The later oxidation of disseminated and vein-related sulfides above the paleo-water table caused a remobilization of Au and Cu that resulted in the deposition of native Au associated with quartz, barite, and metal oxides around the paleo-water table while also transforming chalcopyrite to secondary Cu phases in the enriched zone (Fig. 13). We conclude that the Au enrichment of the Profitis Ilias mountain is genetically subdivided into an upper part (> 400–500 m elevation), where native Au precipitated due to supergene processes, and a lower part (< 300 m), where Au is hosted by abundant base metal sulfides (up to 2 µg/g Au) and Ag-Au-telluride inclusions in early vein pyrite that precipitated during fluid boiling.

In summary, the evolution of the low- to intermediate sulfidation epithermal Profitis Ilias mineralization in combination with the other hydrothermal mineralizations on Milos Island provides unique insights into the transport and precipitation behavior of Au, Ag, Te, and related metal(loid)s by various fluid processes occurring in large, shallow-crustal hydrothermal systems.

Supplementary information The online version contains supplementary material available at https://doi.org/10.1007/s00126-023-01170-2.

Acknowledgements We gratefully acknowledge Melanie Hertel, Stefan Krumm, Helene Brätz, and Frederic Couffignal for performing the XRF, XRD, LA-ICP-MS, and SIMS analyses, respectively. We also thank Marcel Regelous and Bettina Storch for their help during trace element and Pb isotope analysis. We are grateful to David Dolejš and Georges Beaudoin for editing and comments, and to Jon Naden and an anonymous reviewer for their constructive reviews that clearly helped to improve the quality of the manuscript.

Funding Open Access funding enabled and organized by Projekt DEAL. The authors did not receive any funding for conducting this study. The authors have no relevant financial or non-financial interests to disclose.

References

Afifi AM, Kelly WC, Essene EJ (1988) Phase relations among tellurides, sulfides, and oxides: I. Thermochemical data and calculated equilibria. Econ Geol 83:377–394

Ague JJ (2003) Fluid infiltration and transport of major, minor, and trace elements during regional metamorphism of carbonate rocks, Wepawaug Schist, Connecticut, USA. Am J Sci 303:753–816. https://doi.org/10.2475/ajs.303.9.753

Alfieris D (2006) Geological, geochemical and mineralogical studies of shallow submarine epithermal mineralization in an Emergent Volcanic Edifice, at Milos Island (Western Side), Greece. PhD thesis, University of Hamburg, p 294

Alfieris D, Voudouris PC, Spry PG (2013) Shallow submarine epithermal Pb-Zn-Cu-Au-Ag-Te mineralization on western Milos Island, Aegean Volcanic Arc, Greece: mineralogical, geological and geochemical constraints. Ore Geol Rev 53:159–180. https://doi.org/10.1016/j.oregeorev.2013.01.007

Arfè G, Boni M, Mondillo N, Aiello R, Balassone G, Arseneau V, Soyk D (2016) Supergene alteration in the capricornio AU-AG epithermal vein system, Antofagasta Region, Chile. Can Mineral 54:681–706. https://doi.org/10.3749/canmin.1600012

Barnes S-J (2018) Chalcophile Elements. In: White WM (ed) Encyclopedia of Geochemistry. Springer, pp 229–233

Berkenbosch HA, de Ronde CEJ, Ryan CG, McNeill AW, Howard DL, Gemmell JB, Danyushevsky LV, De RCEJ, Ryan CG, McNeill AW, Howard DL, Gemmell JB, Danyushevsky LV (2019) Trace element mapping of copper- and zinc-rich black smoker chimneys from brothers volcano, kermadec arc, using synchrotron radiation XFM and LA-ICP-MS. Econ Geol 114:67–92. https://doi.org/10.5382/econgeo.2019.4620

Börner F, Keith M, Smith DJ, Barry TL, Neumann T, Klemd R (2021) Fingerprinting fluid evolution by trace elements in epithermal pyrite, Vatukoula Au-Te deposit. Fiji. Ore Geol Rev 137:104314. https://doi.org/10.1016/j.oregeorev.2021.104314

Brugger J, Liu W, Etschmann B, Mei Y, Sherman DM, Testemale D (2016) A review of the coordination chemistry of hydrothermal systems, or do coordination changes make ore deposits? Chem Geol 447:219–253. https://doi.org/10.1016/j.chemgeo.2016.10.021

Butt C (1998) Supergene gold deposits. J Aust Geol Geophys 17:89–96

Clark JR, Williams-Jones AE (1990) Analogues of epithermal gold-silver deposition in geothermal well scales. Nature 346:644–645. https://doi.org/10.1038/346644a0

Cooke DR, McPhail DC (2001) Epithermal Au-Ag-Te Mineralization, Acupan, Baguio District, Philippines: numerical simulations of mineral deposition. Econ Geol 96:109–131. https://doi.org/10.2113/gsecongeo.96.1.109

Crerar D, Wood S, Brantley S, Bocarsly A (1985) Chemical controls on solubility of ore-forming minerals in hydrothermal solutions. Can Mineral 23:333–352

Crowe DE, Vaughan RG (1996) Characterization and use of isotopically homogeneous standards for in situ laser microprobe analysis of34S/32S ratios. Am Mineral 81(1–2):187–193. https://doi.org/10.2138/am-1996-1-223

DeMatties TA (2018) Effects of paleoweathering and supergene activity on volcanogenic massive sulfide (VMS) mineralization in the Penokean Volcanic Belt, northern Wisconsin, Michigan and east-central Minnesota, USA: implications for future exploration. Ore Geol Rev 95:216–237. https://doi.org/10.1016/j.oregeorev.2018.02.002

Doebelin N, Kleeberg R (2015) Profex a graphical user interface for the Rietveld refinement program BGMN. J Appl Crystallogr 48:1573–1580. https://doi.org/10.1107/S1600576715014685

Dotsika E, Poutoukis D, Michelot JLL, Raco B (2009) Natural tracers for identifying the origin of the thermal fluids emerging along the Aegean Volcanic arc (Greece): evidence of Arc-Type Magmatic Water (ATMW) participation. J Volcanol Geotherm Res 179:19–32. https://doi.org/10.1016/j.jvolgeores.2008.09.024

Drummond SE, Ohmoto H (1985) Chemical evolution and mineral deposition in boiling hydrothermal systems. Econ Geol 80:126–147. https://doi.org/10.2113/gsecongeo.80.1.126

Einaudi MT, Hedenquist JW, Inan EE (2003) Sulfidation state of fluids in active and extinct hydrothermal systems: transitions from porphyry to epithermal environments. Soc Econ Geol Spec Publ 10:285–314. https://doi.org/10.1006/bbrc.1994.1578

Falkenberg JJ, Keith M, Haase KM, Bach W, Klemd R, Strauss H, Yeo IA, Rubin KH, Storch B, Anderson MO (2021) Effects of fluid boiling on Au and volatile element enrichment in submarine arc-related hydrothermal systems. Geochim Cosmochim Acta 307:105–132. https://doi.org/10.1016/j.gca.2021.05.047

Falkenberg JJ, Keith M, Haase KM, Sporer C, Bach W, Klemd R, Strauss H, Storch B, Peters C, Rubin KH, Anderson MO (2022) Spatial variations in magmatic volatile influx and fluid boiling in the submarine hydrothermal systems of niuatahi caldera, Tonga rear-arc. Geochem Geophys Geosyst 23:e2021GC010259. https://doi.org/10.1029/2021GC010259

Frenzel M, Hirsch T, Gutzmer J (2016) Gallium, germanium, indium, and other trace and minor elements in sphalerite as a function of deposit type - A meta-analysis. Ore Geol Rev 76:52–78. https://doi.org/10.1016/j.oregeorev.2015.12.017

Frenzel M, Voudouris P, Cook NJ, Ciobanu CL, Gilbert S, Wade BP (2021) Evolution of a hydrothermal ore-forming system recorded by sulfide mineral chemistry: a case study from the Plaka Pb–Zn–Ag Deposit, Lavrion, Greece. Miner Depos 57(3):417–438. https://doi.org/10.1007/s00126-021-01067-y

Fytikas M, Innocenti F, Kolios N, Manetti P, Mazzuoli R, Poli G, Rita F, Villari L (1986) Volcanology and petrology of volcanic products from the island of Milos and neighbouring islets. J Volcanol Geotherm Res 28:297–317

Goldfarb RJ, Hofstra AH, Simmons SF (2016) Critical elements in carlin, epithermal, and orogenic gold deposits. In: Verplanck PL, Hitzmann MW (eds) Rare earth and critical elements in ore deposits. Soc Econ Geol

González-Partida E, Carrillo-Chávez A, Levresse G, Tello-Hinojosa E, Venegas-Salgado S, Ramirez-Silva G, Pal-Verma M, Tritlla J, Camprubi A (2005) Hydro-geochemical and isotopic fluid evolution of the Los Azufres geothermal field, Central Mexico. Appl Geochemistry 20:23–39. https://doi.org/10.1016/j.apgeochem.2004.07.006

Govindaraju K (1994) 1994 Compilation of working values and sample description for 383 geostandards. Geostand Newslett 18:1–158. https://doi.org/10.1046/j.1365-2494.1998.53202081.x-i1

Grant HLJ, Hannington MD, Hardardóttir V, Fuchs SH, Schumann D (2020) Trace metal distributions in sulfide scales of the seawater-dominated Reykjanes geothermal system: constraints on sub-seafloor hydrothermal mineralizing processes and metal fluxes. Ore Geol Rev 116:103145. https://doi.org/10.1016/j.oregeorev.2019.103145

Grasemann B, Huet B, Schneider DA, Rice AHN, Lemonnier N, Tschegg C (2018) Miocene postorogenic extension of the Eocene synorogenic imbricated Hellenic subduction channel: New constraints from Milos (Cyclades, Greece). Bull Geol Soc Am 130:238–262. https://doi.org/10.1130/B31731.1

Grundler PV, Brugger J, Etschmann BE, Helm L, Liu W, Spry PG, Tian Y, Testemale D, Pring A (2013) Speciation of aqueous tellurium(IV) in hydrothermal solutions and vapors, and the role of oxidized tellurium species in Te transport and gold deposition. Geochim Cosmochim Acta 120:298–325. https://doi.org/10.1016/j.gca.2013.06.009

Guilbert JM, Park CF (2007) The Geology of Ore Deposits. Waveland Press

Hedenquist JW, Arribas A, Gonzalez-Urien E (2000) Exploration for epithermal gold deposits. Soc Econ Geol Rev 13(245–277):07410123

Hedenquist JW, Lowenstern JB (1994) The role of magmas in the formation of hydrothermal ore deposits. Nature 370:519–527

Heinrich CA (2007) Fluid-fluid interactions in magmatic-hydrothermal ore formation. Rev Mineral Geochem 65:363–387. https://doi.org/10.2138/rmg.2007.65.11

Hemley JJ, Cygan GL, Fein JB, Robinson GR, D'Angelo WM (1992) Hydrothermal ore-forming processes in the light of studies in rock-buffered systems: I, Iron-copper-zinc-lead sulfide solubility relations. Econ Geol 87:1–22. https://doi.org/10.2113/gsecongeo.87.1.1

Hemley JJ, Hunt JP (1992) Hydrothermal ore-forming processes in the light of studies in rock-buffered systems; II, Some general geologic applications. Econ Geol 87:23–43. https://doi.org/10.2113/gsecongeo.87.1.23

Herzig PM, Hannington MD, Arribas A (1998) Sulfur isotopic composition of hydrothermal precipitates from the Lau back-arc: implications for magmatic contributions to seafloor hydrothermal systems. Miner Depos 33:226–237. https://doi.org/10.1007/s001260050143

Huston DL, Sie SH, Suter GF, Cooke DR, Both RA (1995) Trace elements in sulfide minerals from eastern Australian volcanic-hosted massive sulfide deposits; Part I, Proton microprobe analyses of pyrite, chalcopyrite, and sphalerite, and Part II, Selenium levels in pyrite; comparison with delta 34 S values and. Econ Geol 90:1167–1196. https://doi.org/10.2113/gsecongeo.90.5.1167

Ishikawa Y, Sawaguchi T, Iwya S (1976) Delineation of prospecting targets for Kuroko deposits based on modes of volcanism of underlying dacite and alteration haloes. Min Geol 26:105–117. https://doi.org/10.11456/shigenchishitsu1951.26.105

Kadel-Harder IM, Spry PG, Layton-Matthews D, Voinot A, von der Handt A, McCombs AL (2020) Paragenetic relationships between low- and high-grade gold mineralization in the Cripple Creek Au-Te deposit, Colorado: trace element studies of pyrite. Ore Geol Rev 127:103847. https://doi.org/10.1016/j.oregeorev.2020.103847

Keith M, Haase KM, Klemd R, Smith DJ, Schwarz-Schampera U, Bach W (2018a) Constraints on the source of Cu in a submarine magmatic-hydrothermal system, Brothers volcano, Kermadec island arc. Contrib Mineral Petrol 173:40. https://doi.org/10.1007/s00410-018-1470-5

Keith M, Smith DJ, Doyle K, Holwell DA, Jenkin GRT, Barry TL, Becker J, Rampe J (2020) Pyrite chemistry: a new window into Au-Te ore-forming processes in alkaline epithermal districts, Cripple Creek, Colorado. Geochim Cosmochim Acta 274:172–191. https://doi.org/10.1016/j.gca.2020.01.056

Keith M, Smith DJ, Jenkin GRT, Holwell DA, Dye MD (2018b) A review of Te and Se systematics in hydrothermal pyrite from precious metal deposits: insights into ore-forming processes. Ore Geol Rev 96:269–282. https://doi.org/10.1016/j.oregeorev.2017.07.023

Kilias SP, Naden J, Cheliotis I, Shepherd TJ, Constandinidou H, Crossing J, Simos I (2001) Epithermal gold mineralisation in the active Aegen volcanic arc: the Profitis Ilias deposits, Milos Island, Greece. Miner Depos 36:32–44. https://doi.org/10.1007/s001260050284

Klose L, Keith M, Hafermaas D, Kleint C, Bach W, Diehl A, Wilckens F, Peters C, Strauss H, Klemd R, van Geldern R, Haase KM, Koschinsky A (2021) Trace element and isotope systematics in vent fluids and sulphides from Maka Volcano, North Eastern Lau spreading centre: insights into three-component fluid mixing. Front Earth Sci 9:1–26. https://doi.org/10.3389/feart.2021.776925

Large RR, Gemmell JB, Paulick H, Huston DL (2001) The alternation box plot: a simple approach to understanding the relationship between alteration mineralogy and lithogeochemistry associated with volcanic-hosted massive sulfide deposits. Econ Geol 96:957–971. https://doi.org/10.2113/gsecongeo.96.5.957

Liakopoulos A, Katerinopoulos A, Markopoulos T, Boulegue J (1991) A mineralogical petrographic and geochemical study of samples from wells in the geothermal field of Milos Island (Greece). Geothermics 20:237–256. https://doi.org/10.1016/0375-6505(91)90035-T

Marini L, Moretti R, Accornero M (2011) Sulfur isotopes in magmatic-hydrothermal systems, melts, and magmas. Rev Mineral Geochemistry 73:423–492. https://doi.org/10.2138/rmg.2011.73.14

Marschik R, Bauer T, Hensler A-SS, Skarpelis N, Hölzl S (2010) Isotope geochemistry of the Pb-Zn-Ba(-Ag-Au) mineralization at Triades-Galana, Milos Island, Greece. Resour Geol 60:335–347. https://doi.org/10.1111/j.1751-3928.2010.00139.x

Martin AJ, Keith M, Parvaz DB, Mcdonald I, Boyce AJ, McFall KA, Jenkin GRTT, Strauss H, MacLeod CJ, Nordbayern G, Nürnberg UE (2020) Effects of magmatic volatile influx in mafic VMS hydrothermal systems: evidence from the Troodos ophiolite. Cyprus. Chem Geol 531:119325. https://doi.org/10.1016/j.chemgeo.2019.119325

Maslennikov VV, Maslennikova SP, Large RR, Danyushevsky LV (2009) Study of trace element zonation in vent chimneys from the Silurian Yaman-Kasy volcanic-hosted massive sulfide deposit (Southern Urals, Russia) using Laser Ablation-Inductively Coupled Plasma Mass Spectrometry (LA-ICPMS). Econ Geol 104:1111–1141. https://doi.org/10.2113/gsecongeo.104.8.1111

Mathieu L (2018) Quantifying hydrothermal alteration: a review of methods. Geosciences 8:245. https://doi.org/10.3390/geosciences8070245

McKibben MA, Eldridge CS (1990) Radical sulfur isotope zonation of pyrite accompanying boiling and epithermal gold deposition; a SHRIMP study of the Valles Caldera, New Mexico. Econ Geol 85:1917–1925. https://doi.org/10.2113/gsecongeo.85.8.1917

Miles J (2021) The hydrothermal evolution of Milos Island in space and time: an example of a young emergent volcanic edifice. PhD thesis, University of Bristol, p 326

Milési JP, Marcoux E, Sitorus T, Simandjuntak M, Leroy J, Bailly L (1999) Pongkor (West Java, Indonesia): a pliocene supergene-enriched epithermal Au-Ag-(Mn) deposit. Miner Depos 34:131–149. https://doi.org/10.1007/s001260050191

Naden J, Kilias SP, Darbyshire DPFF (2005) Active geothermal systems with entrained seawater as modern analogs for transitional volcanic-hosted massive sulfide and continental magmato-hydrothermal mineralization: the example of Milos Island, Greece. Geology 33:541–544. https://doi.org/10.1130/G21307.1

Naden J, Kilias SP, Leng MJ, Cheliotis I, Shepherd TJ (2003) Do fluid inclusions preserve δ18O values of hydrothermal fluids in epithermal systems over geological time? Evidence from paleo- and modern geothermal systems, Milos Island, Aegean Sea. Chem Geol 197:143–159. https://doi.org/10.1016/S0009-2541(02)00289-9

Nestmeyer M, Keith M, Haase KM, Klemd R, Voudouris P, Schwarz-Schampera U, Strauss H, Kati M, Magganas A (2021) Trace element signatures in pyrite and marcasite from shallow marine island arc-related Hydrothermal Vents, Calypso Vents, New Zealand, and Paleochori Bay, Greece. Front Earth Sci 9:1–18. https://doi.org/10.3389/feart.2021.641654

Páez GN, Ruiz R, Guido DM, Ríos FJ, Subias I, Recio C, Schalamuk IB (2016) High-grade ore shoots at the Martha epithermal vein system, Deseado Massif, Argentina: the interplay of tectonic, hydrothermal and supergene processes in ore genesis. Ore Geol Rev 72:546–561. https://doi.org/10.1016/j.oregeorev.2015.07.026

Plotinskaya OY, Kovalenker VA, Seltmann R, Stanley CJ (2006) Te and Se mineralogy of the high-sulfidation Kochbulak and Kairagach epithermal gold telluride deposits (Kurama Ridge, Middle Tien Shan, Uzbekistan). Mineral Petrol 87:187–207. https://doi.org/10.1007/s00710-006-0130-z

Pokrovski GS, Borisova AY, Bychkov AY (2013) Speciation and transport of metals and metalloids in geological vapors. Rev Mineral Geochem 76:165–218. https://doi.org/10.2138/rmg.2013.76.6

Reed M, Spycher N (1984) Calculation of pH and mineral equilibria in hydrothermal waters with application to geothermometry and studies of boiling and dilution. Geochim Cosmochim Acta 48:1479–1492

Reed MH, Palandri J (2006) Sulfide mineral precipitation from hydrothermal fluids. Rev Mineral Geochem 61:609–631. https://doi.org/10.2138/rmg.2006.61.11

Regelous M, Regelous A, Grasby SE, Bond DPG, Haase KM, Gleißner S, Wignall PB (2020) Tellurium in late permian-early triassic sediments as a proxy for Siberian Flood Basalt Volcanism. Geochem Geophys Geosyst 21:1–15. https://doi.org/10.1029/2020GC009064

Reich M, Kesler SE, Utsunomiya S, Palenik CS, Chryssoulis SL, Ewing RC (2005) Solubility of gold in arsenian pyrite. Geochim Cosmochim Acta 69:2781–2796. https://doi.org/10.1016/j.gca.2005.01.011

Richards JP (2011) Magmatic to hydrothermal metal fluxes in convergent and collided margins. Ore Geol Rev 40:1–26. https://doi.org/10.1016/j.oregeorev.2011.05.006

Román N, Reich M, Leisen M, Morata D, Barra F, Deditius AP (2019) Geochemical and micro-textural fingerprints of boiling in pyrite. Geochim Cosmochim Acta 246:60–85. https://doi.org/10.1016/j.gca.2018.11.034

Saunders JA, Brueseke ME (2012) Volatility of Se and Te during subduction-related distillation and the geochemistry of epithermal ores of the Western United States. Econ Geol 107:165–172. https://doi.org/10.2113/econgeo.107.1.165

Schaarschmidt A, Haase KM, Klemd R, Keith M, Voudouris PC, Alfieris D, Strauss H, Wiedenbeck M (2021) Boiling effects on trace element and sulfur isotope compositions of sulfides in shallow-marine hydrothermal systems: evidence from Milos Island. Greece. Chem Geol 583:120457. https://doi.org/10.1016/j.chemgeo.2021.120457

Schaarschmidt A, Klemd R, Regelous M, Voudouris PC, Melfos V, Haase KM (2021) The formation of shoshonitic magma and its

relationship to porphyry-type mineralisation: the Maronia pluton in NE Greece. Lithos 380–381:105911. https://doi.org/10.1016/j.lithos.2020.105911

Schmidt K, Koschinsky A, Garbe-Schönberg D, de Carvalho LM, Seifert R (2007) Geochemistry of hydrothermal fluids from the ultramafic-hosted Logatchev hydrothermal field, 15°N on the Mid-Atlantic Ridge: temporal and spatial investigation. Chem Geol 242:1–21. https://doi.org/10.1016/j.chemgeo.2007.01.023

Scott SD (1983) Chemical behaviour of sphalerite and arsenopyrite in hydrothermal and metamorphic environments. Mineral Mag 47:427–435. https://doi.org/10.1180/minmag.1983.047.345.03

Seward TM, Williams-Jones AE, Migdisov AA (2014) The chemistry of metal transport and deposition by ore-forming hydrothermal fluids. Treatise on Geochemistry, 2nd editio. Elsevier, Oxford, pp 29–57

Shanks WC, Bischoff JL, Rosenbauer RJ (1981) Seawater sulfate reduction and sulfur isotope fractionation in basaltic systems: Interaction of seawater with fayalite and magnetite at 200–350°C. Geochim Cosmochim Acta 45:1977–1995. https://doi.org/10.1016/0016-7037(81)90054-5

Sillitoe RH (2005) Supergene oxidized and enriched porphyry copper and related deposits. In: Hedenquist JW, Thompson JFH, Goldfarb RJ, Richards JP (eds) One hundredth anniversary volume. Soc Econ Geol

Simmons SF, Brown KL, Tutolo BM (2016) Hydrothermal transport of Ag, Au, Cu, Pb, Te, Zn, and other metals and metalloids in New Zealand geothermal systems: spatial patterns, fluid-mineral equilibria, and implications for epithermal mineralization. Econ Geol 111:589–618. https://doi.org/10.2113/econgeo.111.3.589

Smith DJJ, Naden J, Miles A-JJ, Bennett H, Bicknell SHH (2018) Mass wasting events and their impact on the formation and preservation of submarine ore deposits. Ore Geol Rev 97:143–151. https://doi.org/10.1016/j.oregeorev.2018.05.008

Steadman JA, Large RR, Olin PH, Danyushevsky LV, Meffre S, Huston D, Fabris A, Lisitsin V, Wells T (2021) Pyrite trace element behavior in magmatic-hydrothermal environments: an LA-ICPMS imaging study. Ore Geol Rev 128:103878. https://doi.org/10.1016/j.oregeorev.2020.103878

Stewart AL, McPhie J (2006) Facies architecture and Late Pliocene - Pleistocene evolution of a felsic volcanic island, Milos, Greece. Bull Volcanol 68:703–726. https://doi.org/10.1007/s00445-005-0045-2

Stouraiti C, Pantziris I, Vasilatos C, Kanellopoulos C, Mitropoulos P, Pomonis P, Moritz R, Chiaradia M (2017) Ophiolitic remnants from the upper and intermediate structural unit of the Attic-Cycladic Crystalline Belt (Aegean, Greece): fingerprinting geochemical affinities of magmatic precursors. Geosciences 7:14. https://doi.org/10.3390/geosciences7010014

Swinkels LJ, Schulz-Isenbeck J, Frenzel M, Gutzmer J, Burisch M (2021) Spatial and temporal evolution of the Freiberg epithermal Ag-Pb-Zn district, Germany. Econ Geol 116:1649–1667. https://doi.org/10.5382/ECONGEO.4833

Taylor SR, McLennan SM (1985) The continental crust: its composition and evolution. Blackwell Scientific Pub, United States

Valsami-Jones E, Baltatzis E, Bailey EH, Boyce AJ, Alexander JL, Magganas A, Anderson L, Waldron S, Ragnarsdottir KV (2005) The geochemistry of fluids from an active shallow submarine hydrothermal system: Milos Island, Hellenic Volcanic Arc. J Volcanol Geotherm Res 148:130–151. https://doi.org/10.1016/j.jvolgeores.2005.03.018

Wang S, Li C, Li B, Dang Y, Ye J, Zhu Z, Zhang L, Shi X (2022) Constraints on fluid evolution and growth processes of black smoker chimneys by pyrite geochemistry: a case study of the Tongguan hydrothermal field. South Mid-Atlantic Ridge. Ore Geol Rev 140:104410. https://doi.org/10.1016/j.oregeorev.2021.104410

Wedepohl KH (1995) The composition of the continental crust. Geochim Cosmochim Acta 59:1217–1232. https://doi.org/10.1016/0016-7037(95)00038-2

White NC, Hedenquist JW (1990) Epithermal environments and styles of mineralization: variations and their causes, and guidelines for exploration. J Geochemical Explor 36:445–474. https://doi.org/10.1016/0375-6742(90)90063-G

Wind SC, Schneider DA, Hannington MD, McFarlane CRM (2020) Regional similarities in lead isotopes and trace elements in galena of the Cyclades Mineral District, Greece with implications for the underlying basement. Lithos 366–367:105559. https://doi.org/10.1016/j.lithos.2020.105559

Zelenski M, Simakin A, Taran Y, Kamenetsky VS, Malik N (2021) Partitioning of elements between high-temperature, low-density aqueous fluid and silicate melt as derived from volcanic gas geochemistry. Geochim Cosmochim Acta 295:112–134. https://doi.org/10.1016/j.gca.2020.12.011

Zhou X, Kuiper K, Wijbrans J, Boehm K, Vroon P (2021) Eruptive history and 40Ar/39Ar geochronology of the Milos volcanic field, Greece. Geochronology 3:273–297. https://doi.org/10.5194/gchron-3-273-2021